Assessment of seasonal Borehole Thermal Energy Storage in the seawater intrusion region of a carbonate aquifer

Nicola Pastore [a,*], Claudia Cherubini [b]

[a] *Polytechnic of Bari, Department of Civil, Environmental and Structural Engineering and Chemistry (DICATECh), via E. Orabona 4, Bari 70125, Italy*
[b] *Department of Physics and Earth Sciences, University of Ferrara, via Saragat 1, Ferrara 44122, Italy*

ARTICLE INFO

ABSTRACT

In coastal areas the seawater intrusion region underlying freshwater aquifers represents a low quality but wide and deep geo resource. Seasonal thermal energy storage and recovery is an important component of district heating and cooling system to manage renewable energy fluctuations, such as solar irradiance or waste heat from industrial processes, and the corresponding mismatch of thermal energy demand and supply. A numerical tool to evaluate the performance of seasonal Borehole Thermal Energy Storage (BTES) system to store and recover solar energy in the seawater intrusion region, underlying the shallow freshwater aquifer and with thermally and hydraulically insulated upper borehole section is developed and applied to the coastal carbonate aquifer of the metropolitan area of Bari (Italy). The hourly thermal demand of the University Sport Centre of Bari is used as benchmark. The design and performance of the BTES system is strongly dependent on the geological and hydrogeological context as well as on the environmental and operational conditions. The aquifer characterization suggests to locate BTES zone at a depth higher than 100 m from the freshwater – saltwater interface where carbonate unit appears less fractured and karstified showing a value of bulk permeability less than $10^{-12}\,\mathrm{m}^2$ and the groundwater flow is slow ($\sim 10^{-3}\,\mathrm{md}^{-1}$). Rayleigh number criterion is used as constraint to determine the maximum heat storage temperature ($\sim 70°C$) in order to preserve the lateral thermal stratification and the thermal impact on the shallow freshwater resource. A novel mathematical and computational model is developed to help the design of BTES system and to evaluate its efficiency. The results indicate that the thermal losses within thermally insulated zone influence the effective thermal recovery factor which, according to the baseline scenario, is equal to 47% after five years of operation. The heat energy production of the solar heating system, covers the heat demand with percentage range of 79–117%. The location of BTES in deep seawater region attenuates the decreases of efficiency due to the groundwater flow which became significant at specific discharge around $10^{-2}\,\mathrm{md}^{-1}$. Changing the operation schedule with a shorter heating storage period increases the thermal recovery factor of the BTES of 11.19% after five years of operation, but at the same time the trend of the heat energy production shows a surplus during the midseason and deficit during the winter and summer season respect to the thermal demand. Great care must be taken on the maximum heat storage temperature. A low heat storage temperature ensures a wider safety margin with regards to the thermal stratification and the thermal impact on the shallow aquifer. Anyway, a decrease of 10°C on the maximum heat storage temperature produces a deficit of the heat production respect to the thermal demand in the range of 15%–21%.

1. Introduction

The heating and cooling of water and air represent an important item of the energy consumption of urban and industrial settlements with enormous economic, environmental, and social costs due to systemic inefficiencies. The Districts of Heating and Cooling (DHC), given their high energy efficiency, represent the most effective and efficient

solution. When DHC use renewable energy sources, they can significantly reduce greenhouse gas emissions and dependence on fossil fuels, increasing the resilience and sustainability of urban and industrial areas with an optimal and cost-effective design (Werner, 2017).

Solar irradiance plays an important role in renewable DHC, providing a great potential for electrical and heat energy production (Nouri et al., 2019). Besides, solar irradiance fluctuates daily and

seasonally (Ma and Wang, 2020). In order to attenuate this intermittent behavior, thermal energy storage at seasonal (long-term), monthly (mid-term) and diurnal (short-term) time scale is needed (Sakellariou et al., 2021).

In this context, the geothermal energy storage and recovery concept provides large-scale and seasonally long-term heat and cooling storage when heat and cooling surplus is available. The solar irradiance, available discontinuously throughout the year, can be accumulated within the geothermal reservoir during its peak of production. Subsequently, the accumulated heat will be recovered and transferred to urban, agricultural and industrial users with huge environmental and economic benefits (Panja et al., 2021).

From the technical and economical points of view, both Aquifer Thermal Energy Storage (ATES) (Nordell et al., 2015; Zeghici et al., 2015; Winterleitner et al., 2018; Bloemendal and Olsthoorn, 2018; Burns et al., 2020; Sheldon et al., 2021) and Borehole Thermal Energy Storage (BTES) (Moradi et al., 2015; Cui et al., 2015; Nguyen et al., 2017; Welsch et al., 2018; Abbas et al., 2020; Beckers et al., 2022) systems are two promising technologies for long-term storage. ATES and BTES, compared to other storage technologies such as water tanks, present the advantage of not taking up much surface area and they are particularly indicated for densely populated urban areas (Schulte et al., 2019).

In ATES systems, seasonal thermal storage occurs in aquifers with high yield by means of two -or multiple of two- separated wells. ATES necessarily induced forced groundwater flow in the aquifer between the injection and extraction wells. Then advection due to forced groundwater flow plays an important role on the seasonal storage in ATES system. Generally, ATES operates in shallow aquifers with temperature $< 25°C$ due to policy and regulation restrictions (Schüppler et al., 2019). Then such system does not permit the direct use of heat, but a heat pump is needed. Moreover, other renewable technologies such as thermal solar collectors, biomass, waste to energy or industrial heat waste present higher working temperatures that are not compatible with shallow ATES system. To enable higher storage temperatures ($> 50°C$), greater depths are needed, and great care must be taken in identifying a suitable site for long term high temperature ATES system. Deep aquifers with high porosity and permeability are crucial in order to obtain economic benefits (Panja et al., 2021).

BTES system is installed in the underground that can range from unconsolidated geological media to rock formations with or without groundwater. In BTES system, in order to obtain the lateral thermal stratification, heat conduction must be the main heat transport mechanism. The optimized configuration provides several hydraulic circuits composed of several vertical borehole heat exchangers (BHEs) linking in series. The circuits are disposed along radials connecting the inner and outer headers in order to favor lateral thermal stratification (Skarphagen et al., 2019). In the storage season, the hot heat carrier fluid is directed towards the core of the BTES, which is warmed to the highest possible temperature, and then radially outwards, progressively warming the outer zone. Conversely, in the recovery season, the cold heat carrier fluid flows from the outer header first and progressively inwards towards the inner header.

The hot carrier fluid that circulates within the BTES is not directly in contact with aquifers. Anyway, due to the working temperature of DHC that are at least above $50°C$, the thermal impact can be significant, especially for a shallow aquifer used for extraction of drinking water. Therefore, in order to avoid these hydrogeological and environmental constraints, a deeper BHE can be used with an insulated upper borehole section avoiding the thermal impact on shallow sensitive aquifers (Welsh et al., 2016; Schulte et al., 2016a, 2016b).

In coastal areas, the saltwater regions underlying coastal freshwater represent largely undeveloped relatively low-quality resources that, being also wide and deep, offer a great potential for application of deep ATES or BTES systems with relatively high temperature (~50°C). Naturally, saltwater regions are poorly connected with the above

shallow freshwater resource. They are characterized by low flow rates and long residence times along the flow path (Burns et al., 2020). Therefore the 'cargo effect' due to the regional groundwater flow that tends to sweep away the accumulated heat along the direction of the groundwater flow does not occur (Skarphagen et al., 2019).

The increase in temperature in saltwater region can reduce the density contrast between fresh and saline water favoring the retreat of the freshwater-seawater interface seaward. Nevertheless, great care must be taken on the possibility of saltwater - freshwater mixing. This environmental constraint can limit the economic benefits of the seasonal thermal storage systems.

BTES appears more affordable respect to ATES for hydrogeological context characterized by low porosity and low permeability. In such context, the efficiency of injection and extraction wells of the ATES system is reduced Conversely, in BTES system the natural convection due to the temperature gradient is not favored permitting the lateral thermal stratification even for high temperature ($>50°C$).

The efficiency of the BHEs, measured in terms of their thermal resistance (Spitler at al., 2016), is one of the key parameters for the optimum design and planning the BTES system. A low value of the BHE thermal resistance is crucial for a BTES system because it increases the thermal recovery factor defined as the ratio between the heat extracted and heat stored over annual cycle. Different types of BHEs can be realized. According to the state of art, heat exchangers with different shapes can be installed within the borehole. Double U-tube heat exchanger represents the most common competitive cheap technology. Then, the borehole volume around the heat exchanger can be backfilled with thermally enhanced grout with a mixture of bentonite and silica sand that reaches a thermal conductivity value of ~2.0 $Wm^{-1}K^{-1}$.

Generally, numerical modeling of seasonal BTES was carried out using dynamic transient simulator of complex energy system such as TRNSYS (Klein et al., 2017). However, this model does not account for the hydrogeological features and some subsurface heat transfer dynamics such as advection and thermal dispersion. Then subsurface flow and mass and heat transport model such as SEAWAT (Langevin et al., 2008) and FEFLOW (Dierch, 2014) is used to verify and optimize the BTES design.

In this paper a new conceptual, mathematical and numerical method is developed to simulate simultaneously the solar heating plant and the BTES. The models are developed in COMSOL 4.0a environment. A quasi 3d conceptualization is used to represent the three-dimensional subsurface heat transport in several two-dimensional heat transport problems according to the geological and hydrogeological characterization and analysis.

The specific goals of this paper are to:

1) Forecast the thermal response and efficiency of a seasonal BTES system in the seawater intrusion region underlying the shallow freshwater aquifer, using the University Sport Centre of Bari (Italy) as benchmark case.
2) Evaluate the thermal impacts of BTES on the shallow freshwater aquifer by means of the modeling of the thermo hydrogeological behaviour of the aquifer.

After presenting the study site and its climatic, geological and hydrogeological setting, the seasonal BTES and solar heating design is described as well as the details of the developed models. Simulation results highlighted the potential and challenge of the system in terms of its efficiency. The influence of shallow freshwater aquifer is discussed.

2. Materials

2.1. Case study

The University Sport Centre (USC) of Bari (Italy) is selected as benchmark for the assessment of the proposed seasonal solar BTES. The
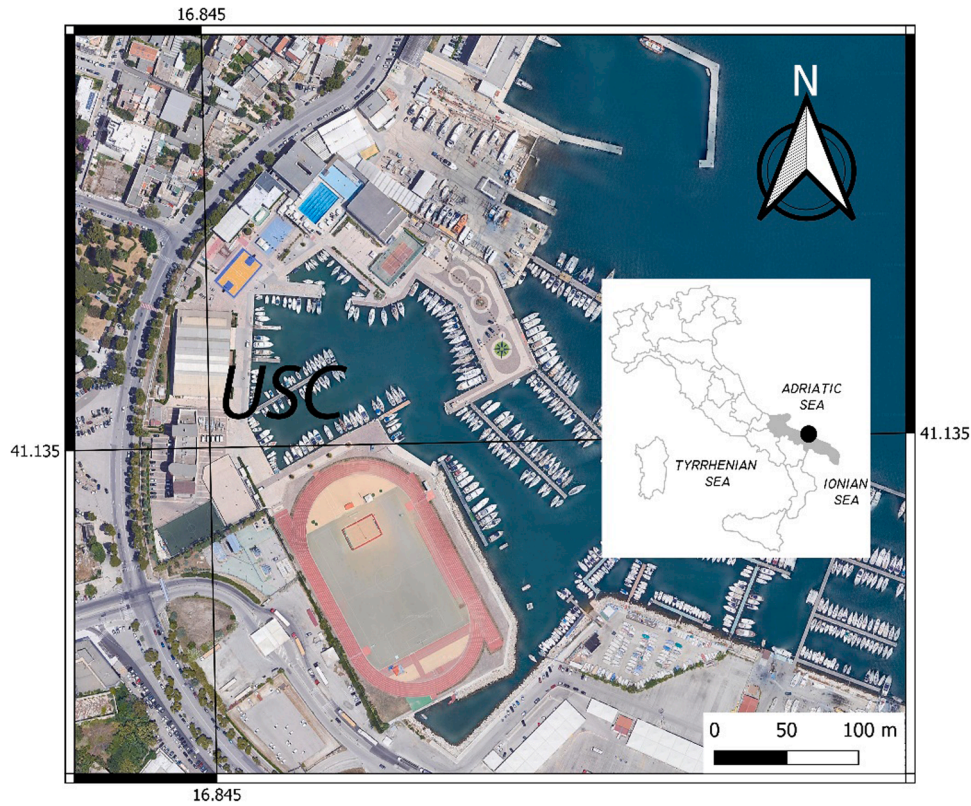
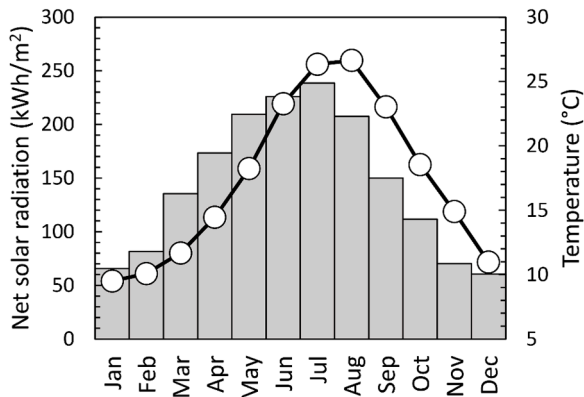Fig. 1. Location of the University Sport Centre (USC) of Bari.

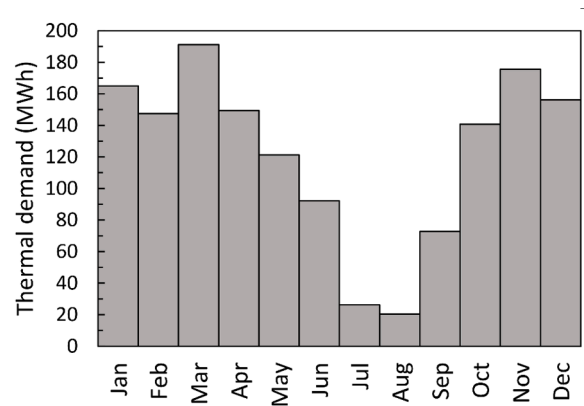Fig. 2. Average Monthly mean temperature and net solar radiation (reference period 2010 – 2020).

Fig. 3. Monthly thermal demand for pool heating and domestic hot water of the USC.

USC is in the urban area of Bari (Fig. 1) close to the Adriatic coast. Bari has a semi-arid climate with an average annual temperature of 17.3°C and mean solar radiation from April to September of 6.57 kWhm^{-2}d^{-1} (Fig. 2).

According to Wang et al. (2019), USC presents a roof area of 4,000 m^2 available for solar thermal collector installation. A volume of 175,000 Sm^3 of natural gas supplies the heat demand of the USC for space heating (142 MWhyr^{-1}), pool heating and Domestic Hot Water (DHW) production (1458 MWhyr^{-1}). In the present work, seasonal solar BTES supplies only the pool heating and DHW production with monthly thermal demand highlighted in Fig. 3.

The space conditioning is supposed covered by a heating/cooling system such as a shallow geothermal heat pump. The hourly frequency of the customers along the week (Fig. 4) is used in order to determine the hourly heat demand for each month.

2.2. Geological and hydrogeological setting

The urban area of Bari falls along the eastern side of the Murgian plateau which is part of the geological and structural domain of the Apulian foreland. The annual average rainfall and potential evapotranspiration presents a value of 540 and 1,063 mmyr^{-1} respectively.

From the morphological point view, the metropolitan area of Bari is a typical coastal Murgian belt, characterized by the presence of three elongated terraces parallel to the coast sloped down to the Adriatic Sea. Paleostream channels or small erosive furrows ("*lame*") develop perpendicular to the terraces. The case study area lies in a morphologically depressed area called Lake of Marisabella (Cherubini et al., 2013) where waters coming from three paleostream channels: *Lama Lamasinata, Lama Lamberti* and *Lama Picone* are conveyed. Actually, these paleostream channels are totally covered by urban areas (Fig. 5).
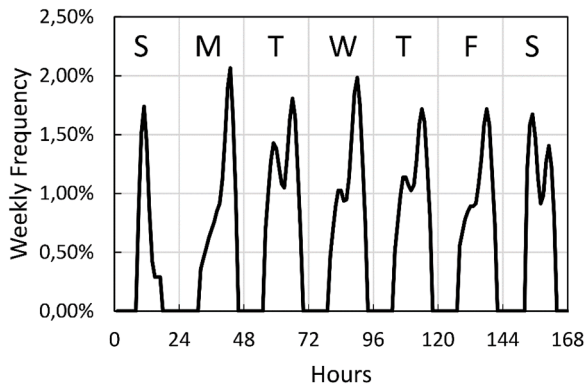
Fig. 4. Average weekly frequency of the customers of the USC.

Geological surveys at location #1 conducted in the urban area of Bari (Fig. 6a) show that, below the topsoil, alluvial deposits (Holocene) are detected above the *Calcareniti di Gravina* formation (lower Pleistocene). The latter is a calcarenitic complex, constituted by dune bioclastic, detrital and sand bar deposits. The *Calcarenite di Gravina* formation is transgressive on the underlying formation, sometimes in angular discordance presenting a variable thickness from few meters to 20 m. Below the calcarenitic strata lies the *Calcare di Bari* formation (Cretaceous) extending in depth for hundreds of meters. From the lithological point view, the facies that characterizes the Cretaceous carbonate basement is constituted by micritic limestone intercalated by dolomitic limestone and dolostone layers. Below 138 m depth, irregular alternations of calcilutites and bioclastic limestone layers are detected.

The latter becomes predominant below 150 m depth where intra-formational calcareous breccias levels are detected also. The carbonate basement results moderately fractured except in local zones where the degree of fracturing and karstification results higher (Figs 6b and 6c). Karst phenomena are not significantly widespread. They are more frequent in the shallow zone. Red soil ("*terra rossa*") due to the residual product of karstification is observed at the fracture walls of the structural discontinuities and joint strata. Moreover, microcavities are more or less diffused, generally occluded by *terra rossa* or calcite recrystallisation. The Rock Quality Designation (RQD) results homogeneous with an average value of 55.59% and a standard deviation of 21.75% (Fig. 6d). Only the first 10 m of the carbonate basement are characterized by a wide range of RQD reaching null values. A systematic correlation between the gamma ray log peak and the presence of intensified fractured or karstified strata are evident (Fig. 6e). Whereas there are no substantial changes of natural radioactivity in correspondence of the detected carbonate facies. Dispersions of natural radioactivity value around an average value characteristic of a stratified carbonate rock is observed.

According to the geological surveys and outcrop observations, the Calcare di Bari formation is characterized by a succession of carbonate beds separated by sub – horizontal marked mechanical discontinuities and affected by two cross – orthogonal sets of perpendicular bedding joints striking N-S and WNW-ESE, respectively with bed parting and bed – unparting behaviour. Joints spacing is directly correlated to the bed
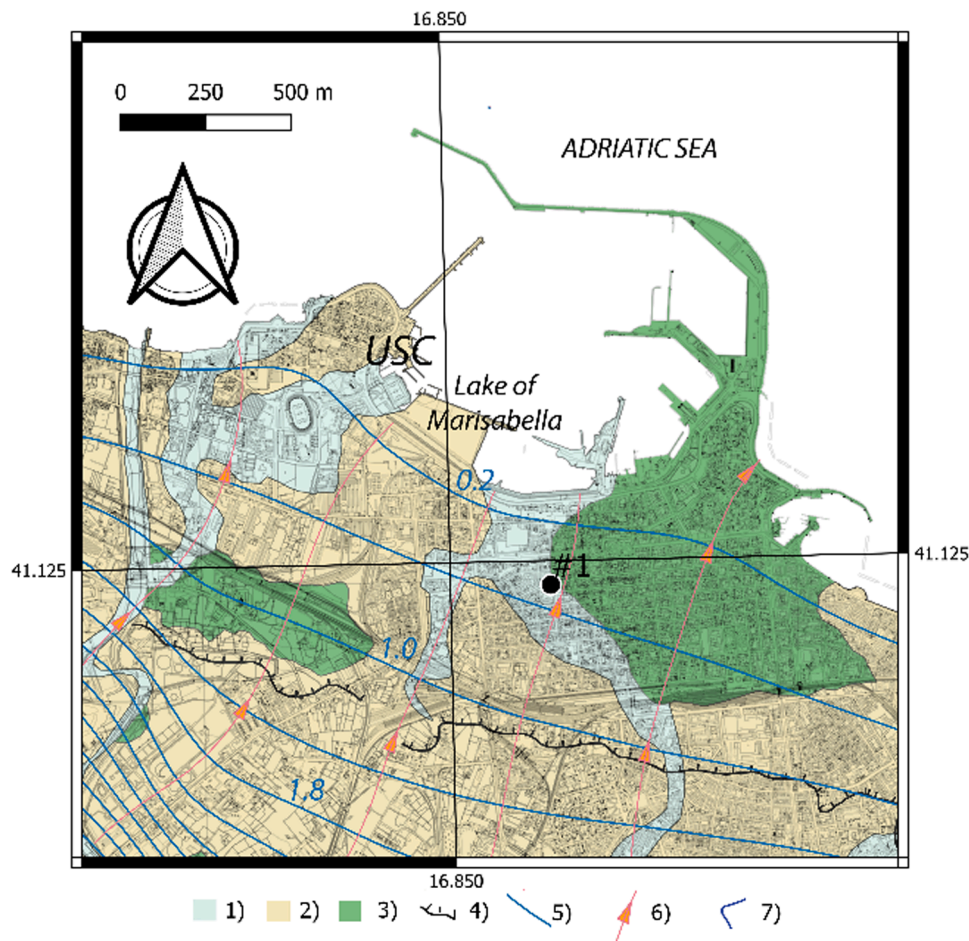
Fig. 5. Geological and hydrogeological setting of study area with location of the USC and the geological survey #1 of Fig. 6. Blue and orange curves are the hydraulic head (m ASML) and the flow paths of freshwater shallow aquifer respectively. Legend: (1) recent deposit (Holocene); (2) Calcareniti di Gravina formation (Lower Pleistocene); (3) Calcare di Bari formation (Cretaceous); (4) escarpments; (5) hydraulic head contour levels (m AMSL); (6) flowpaths.
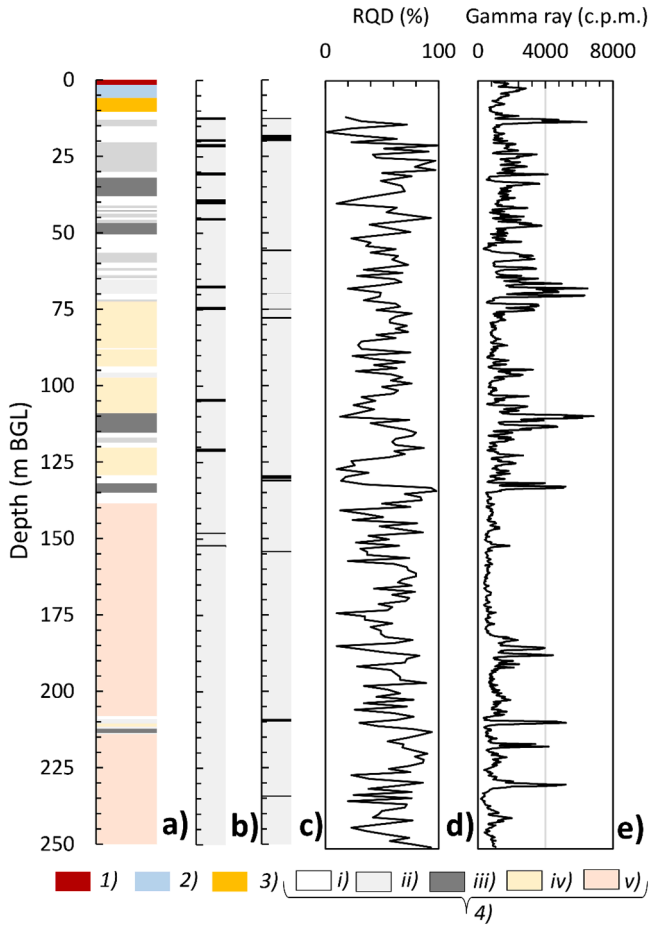
4

Fig. 6. Geological surveys at #1 location. (a) Stratigraphy log. (b) layers with high degree of fracturing (black bar). (C) layers with high degree of karstification (black bar). (c) Rock Quality Designation (RQD) log (%). (d) Gamma ray log (c.p.m.). Legend: (1) Landfill material; (2) Alluvial deposits (Holocene); (3) Calcarenite di Gravina (Lower Pleistocene); (4) Calcare di Bari. Facies: (i) Micritic Limestone; (ii) Dolomitic limestone; (iii) Dolostone; (iv) Calcilutites; (v) Irregular alternation of Calcilutites and Bioclastic Limestone.

Fig. 7. Groundwater characterization at location #1. (a) Electric conductivity (EC) log (μScm^{-1}). (b) Temperature log (°C).

thickness variable in the range 0.15 – 1.20 m.

From the hydrogeological point of view, the study area belongs to the karstic Murgia aquifer. The aquifer recharge occurs mainly in the innermost area up to 40 km to the coast where the limestone unit outcrops continuously and the presence of sinkholes favors the rapid infiltration of water runoff. Recharge occurs mainly in the winter season equal to 30% of the average annual rainfall which varies between 650 mmyr^{-1} in the inland to 540 mmyr^{-1} in the coastal areas (Pieri et al., 2012). Groundwater discharge directly into the Adriatic Sea through springs located in a widespread manner along the coastal areas.

In the study area, groundwater flows in the shallow limestone units under semi-confined condition within fractures and karst channels at variable depth from 40 m Below the Ground Level (BGL) in the most inland zone up to about 12-13 m depth near the coast with hydraulic head values of about 1-2 m Above Mean Sea Level (AMSL) (Grassi et al., 1986). Near to the coast, high tidal fluctuations ($\pm$ 0.5 m AMSL) influence the groundwater level with the oscillations of the hydraulic head in the order of a few decimeters.

Rock porosity is low with values between 1.24% and 5.14%, then pore fluid can be considered stagnant (Borgia et al., 2002). Groundwater flows along preferential channels caused by fracture connectivity with an estimated effective porosity of about ~0.3% (Masciopinto and Palmiotta, 2016).

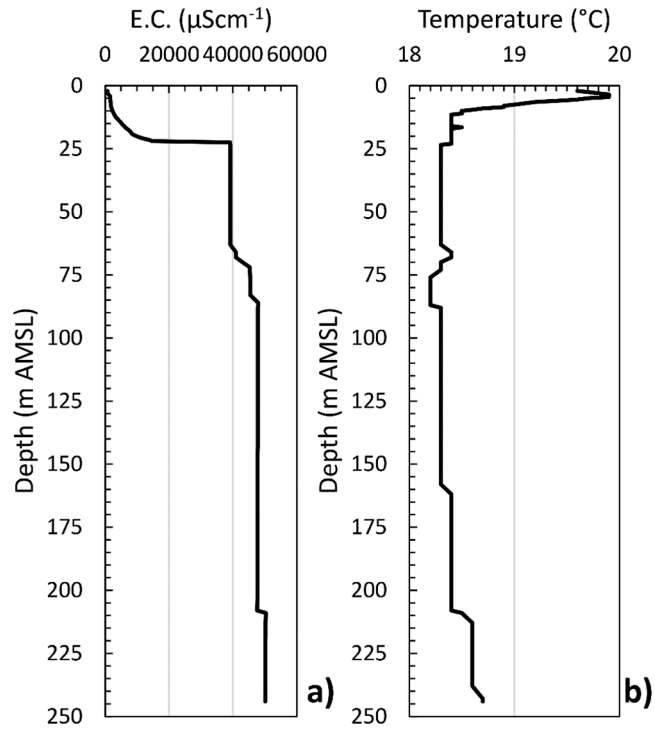A large-scale groundwater flow model was implemented to analyse the hydrogeological features of the shallow limestone aquifer in the metropolitan area of Bari. Details on model conceptualization, governing equation, boundary conditions and validation can be found in Cherubini et al. (2018) and Pastore et al. (2021a). According to these previous studies, in the Metropolitan area of Bari the hydraulic transmissivity varies in the range 0.864–864 m^{2}d^{-1}. Specifically, in correspondence of the study area, the equivalent hydraulic conductivity K_{eq} (LT^{-1}) reaches a value of 100 md^{-1}, whereas a value of the upward recharge Q_f (L^{2}T^{-1}) equal to 0.6 m^{2}d^{-1} can be determined.

In the study area, fresh groundwater floating on an underlying saltwater intrusion region. Along the freshwater – saltwater interface, diffusion causes salt to disperse into the freshwater zone, resulting in a convective (density-driven) circulation through the saltwater wedge.

The electrical conductivity log (Fig. 7a) at #1 shows a marked increase of salt concentration along the depth, passing from 5540 μScm^{-1} to 19458 μScm^{-1} at 24 m BGL reaching a value of 53450 μScm^{-1} at the bottom of borehole (250 m BGL). At #1 located $L = 550$ m from the outflow section (Fig. 5), the transition zone between fresh groundwater and saltwater region is placed around $\zeta(L)$=22 m below the Mean Sea Level (MSL).

According to Masciopinto (2006), the depth below the MSL of the sharp interface at the outflow section $\zeta(0)$, corresponding to the study area can be calculated as:

$$\zeta(0) = \sqrt{\zeta(L)^2 - \frac{2Q_f L}{\alpha K_{eq}}} \qquad (1)$$

Assuming a relative density difference equal to α=0.025 and $\zeta(0) \cong 15$ m.

The Temperature logs (Fig. 7b) show a shallow groundwater temperature affected by seasonal climate variations. As depth increases the water temperature is affected by heat geothermal flux reaching a value slightly above 18°C.
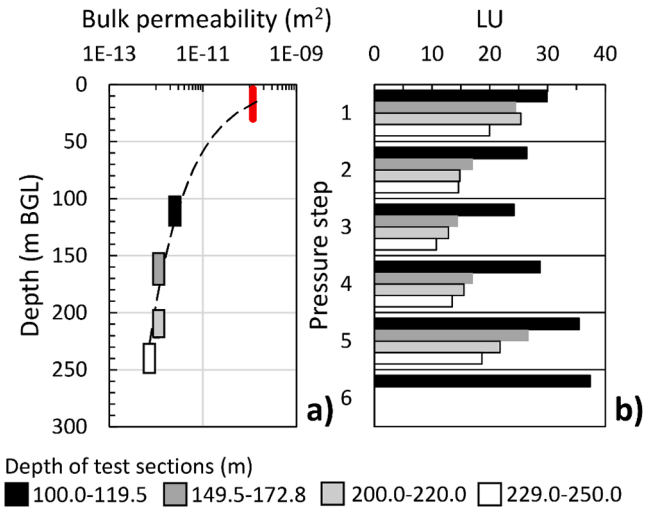
Fig. 8. Hydraulic test results coming from the interpretation of the Lugeon tests. (a) Bulk permeability profile along the depth. Red bar represents the bulk permeability of the shallow aquifer derived by the interpretation of step drawdown test at field site (Cherubini et al., 2018). (b) Lugeon Unit (LU) in correspondence of the relative pressure steps for each test section. Gray scale indicates the depth of Lugeon test.

2.3. Thermal energy potential and heat recovery efficiency

Thermal conductivity values for the Calcare di Bari formation were measured by different authors both in dry and saturated conditions. Niederau et al. (2015) performed a series of laboratory measurements on core samples taken from sites representative of the Cretaceous-Eocene stratigraphy of the Apulian carbonate platform. The main lithologies are dense limestones and dolostones, which show layering and micro-joints. Thermal conductivity of rock matrix k_m ($ML^3T^{-2}K^{-1}$) was measured in both dry and saturated condition, but the data were quite similar in both cases (min: 2.14 $Wm^{-1}K^{-1}$ to max: 2.66 $Wm^{-1}K^{-1}$), due to the low porosity and similar lithology. Using the geometric mean, matrix thermal conductivities were calculated for dry and saturated condition, yielding realistic mean values of 2.48 W $m^{-1}K^{-1}$ (dry) and 2.58 $Wm^{-1}K^{-1}$ (saturated). Di Sipio et al. (2016) carried out direct measurements of thermal conductivity values of the Calcare di Bari formation in laboratory using a specific thermal conductivity analyzer. They found a value for the saturated thermal conductivity of the limestone between 3.7 and 1.5 $Wm^{-1}K^{-1}$ with a mean value equal to 2.5 $Wm^{-1}K^{-1}$. Typical values of density ρ_m (ML^{-3}) and heat capacity c_m ($L^2T^{-2}K^{-1}$) of carbonate rock are 2700 kgm^{-3} and 910 $Jkg^{-1}m^{-3}$ (Robertson, 1988).

The heat recovery efficiency of a BTES system is strongly dependent on the thermal resistance of the BHE, intrinsic permeability of the aquifer and natural groundwater velocity.

We expect that in shallow freshwater aquifer advection represents the main heat transport mechanism, whereas in the saltwater intrusion region natural groundwater flow is slow as a consequence of comparatively low flow rates and long residence times along flow paths that are poorly connected with shallower fresh groundwater systems (Burns et al., 2020).

As outlined by Catolico et al. (2016) the heat recovery efficiency depends on the bulk permeability of fracture rock k_f (L^2). This behaviour is linked with the occurrence of the natural convection due to the temperature gradient. On the assumption that the carbonate rock works as a homogeneous porous medium, according to Nield and Bejan (2013) natural convection becomes dominant when the Rayleigh number (Ra) is higher than its critical value $Ra_c = 4\pi^2$. Ra is determined as:

$$Ra = \frac{\beta_w g k_f L_{BHE}(T_b - T_\infty)}{\mu_w D_m} \tag{2}$$

Where β_w (K^{-1}) and μ_w ($ML^{-1}T^{-1}$) is the thermal expansion coefficient and the viscosity of groundwater, g (LT^{-2}) is the acceleration of gravity, L_{BHE} (L) is the length of the BHE, T_b (K) is the temperature at the borehole wall, T_∞ (K) is the ambient groundwater temperature, D_m (L^2T^{-1}) is the thermal diffusivity of the rock equal to:

$$D_m = \frac{k_m}{\rho_m c_m} \tag{3}$$

The value of Ra depends on the amount of heat loss due to conduction and convection. Conduction is the dominant mode of heat transfer for the lower values of the Rayleigh number. When the Rayleigh number exceeds the critical value, the onset of convection occurs. For Ra values lower than Ra_c, heat propagates in the aquifer mainly through thermal diffusion phenomena, leading to lateral thermal stratification. When Ra overcomes its critical value, natural convection triggers the thermosiphon effect. The hot groundwater leaves the BHE in the higher part attracting ambient groundwater from the fractures at lower depth. The convective process is accompanied by lateral heat loss that attenuates lateral thermal stratification and as a consequence a strong decrease of the heat storage and recovery efficiency should be expected.

3. Methods

The methods in the present work consist of five basic steps: (1) bulk permeability determination in saltwater intrusion region by means of aquifer tests; (2) determination of the specific discharge profile at field site (3) BTES design in saltwater region; (4) solar heating system design (5) conceptual and mathematical model of the seasonal Borehole Thermal Energy Storage System.

3.1. Aquifer tests

Lugeon tests (Vaskou et al., 2019) can be used for assessing the equivalent intrinsic permeability of fractured rock along the depth. The Lugeon test was conducted during the borehole perforation at location *#1* using single packer to isolate a section of borehole for water injection at constant pressure. Four – five constant pressure steps are imposed for each test section of borehole, for a period of 10 minutes as long as the injected flow rate remains steady. For each pressure step the Lugeon unit (*LU*) is determined as (Lancaster-Jones, 1975):

$$LU = \frac{Q_{in}}{PL} \tag{4}$$

Where Q_{in} is the injected flow rate ($Lmin^{-1}$), P is the injection pressure (MPa), L (m) is the length of the test section. Frequently, the pressure – adsorbed flow rate diagrams show a non-linear flow behavior influenced by the presence of the turbulent drag forces. Very high hydraulic gradient can occur at the isolated test section that leads to high velocity flow regime within the fracture network (Zhou et al., 2018). As result *LU* decreases as *P* increases, presenting a small hysteresis between the ascending and descending test phases.

Forchheimer law can be applied in order to describe the observed non – linear flow behaviour (Houben, 2015). With the assumption that in tested fractured rock the flow propagates radially from the borehole axis, the Forchheimer law can be written as:

$$-\frac{\partial p_f}{\partial r} = \frac{\mu_w}{2\pi r \Lambda k_f} Q + \frac{\beta_f \rho_w}{(2\pi r \Lambda)^2} Q^2 \tag{5}$$

Where r (L) is the radial coordinate, Q (L^3T^{-1}) is the injection flow rate, p_f ($ML^{-1}T^{-2}$) is the pressure within the fractured rock, ρ_w (ML^{-3}) is the density of the groundwater, β_f (L^{-1}) is the non – Darcy coefficient, Λ (L)
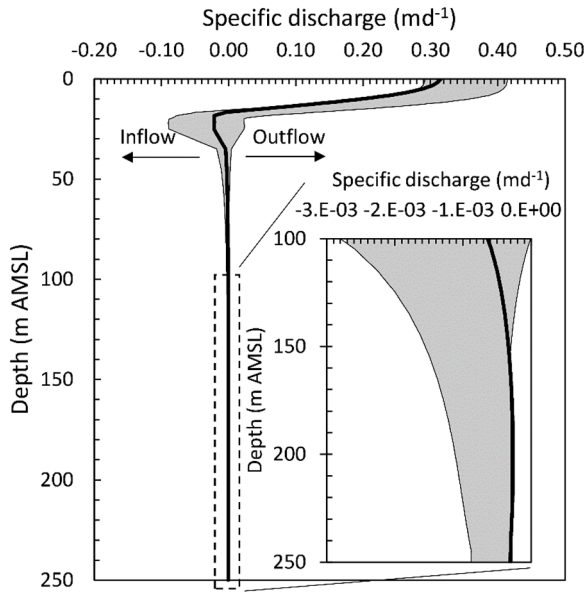
Fig. 9. Specific discharge profile along the depth at steady state (bold curve) and the envelope of the specific discharge during transient condition (gray area) according to the tidal fluctuation obtained from the two – dimensional cross-section numerical model of variable density flow and solute transport.

is the length of the test section.

The steady-state analytical solution of radial flow out from line source on the borehole axis, assuming that the borehole radius r (L) is much lower than the height of the test section L can be written as:

$$dp_f = \frac{\mu_w}{2\pi k_f \Lambda} \ln\left(\frac{R}{r}\right) Q - \frac{\beta_f \rho_w}{(2\pi\Lambda)^2}\left(\frac{1}{R} - \frac{1}{r}\right) Q^2 \qquad (6)$$

Where R (L) is the influence radius which can be set equal to Λ.

Lugeon tests were conducted at different depths in correspondence of the following test sections isolated by single pneumatic packer: 100.0–119.5 m; 149.5–172.8 m; 200.0–220.0 m; 229.0–250.0 m. Different pressure steps were adopted, specifically between 0.047 and 0.47 MPa. The value of the bulk permeability decreases with the depth passing from 1.18×10^{-10} m^2 within the shallow freshwater aquifer to 7.65×10^{-13} at lowest depth (229.0–250.0 m) (Fig. 8a). For all the conducted tests, the values of LU unit decrease as the pressure increases, presenting a small hysteresis between the ascending and descending test phases caused by the presence of a non-linear flow behavior due to turbulent drag forces (Fig. 8b).

3.2. Determination of specific discharge profile in the study area

In order to determine the specific discharge profile in the study area, a two – dimensional cross-sectional numerical model of variable density flow and solute transport (Pu et al., 2020) was set up in COMSOL 4.0a environment. The horizontal axis was aligned along the fresh groundwater flow path at USC (Fig. 1). The conceptual model depicts the carbonate aquifer as a porous geological media with the bulk permeability that varies along the depth according to the results of the hydraulic tests. A value of effective porosity equal to 0.3% was used. The groundwater flows under confined condition. The model domain presents a rectangular shape with depth of 250 m AMSL and a length of 1,000 m. At seaward side, a fixed seawater level (0 m AMSL) was set and a constant concentration of salinity (35 gl^{-1}) was assigned at the inflow zone from

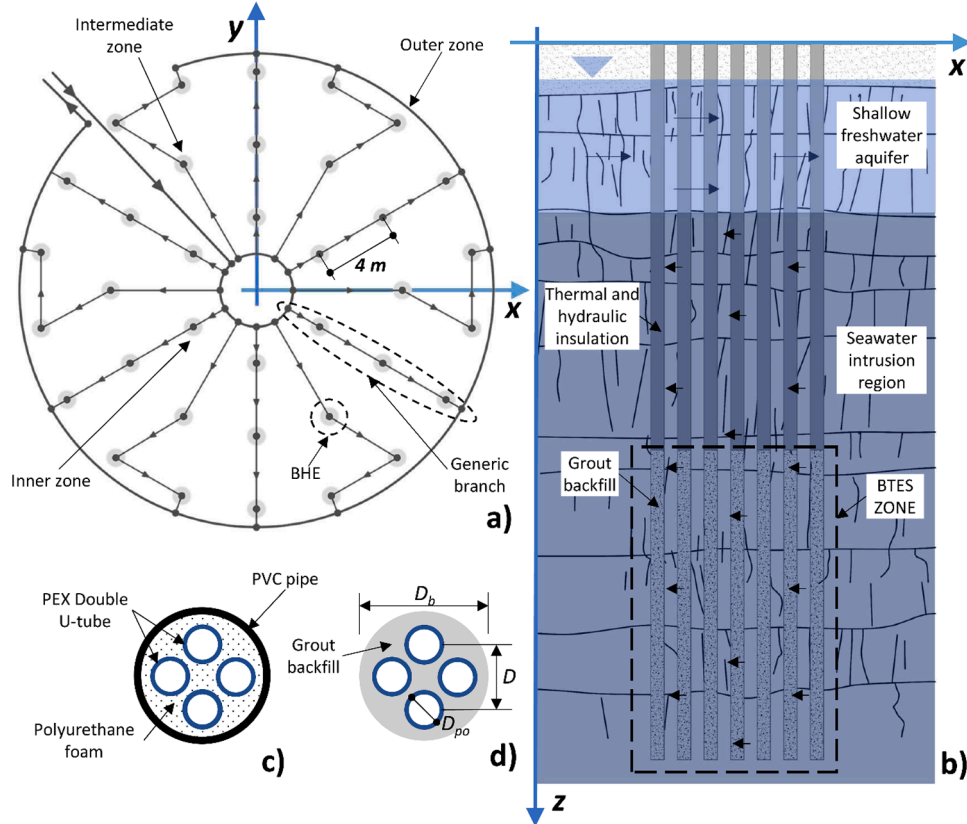**Fig. 10.** Schematic representation of the BTES system: (a) plan view of the BHEs arrangement and their connection to the main headers; (b) vertical view of the BTES system circumvents the problem of the thermal impacts of the shallow aquifer by accessing a less vulnerable seawater intrusion region at higher depth; (c) BHE section at the thermal and hydraulic insulation zone; (d) BHE section at BTES zone.
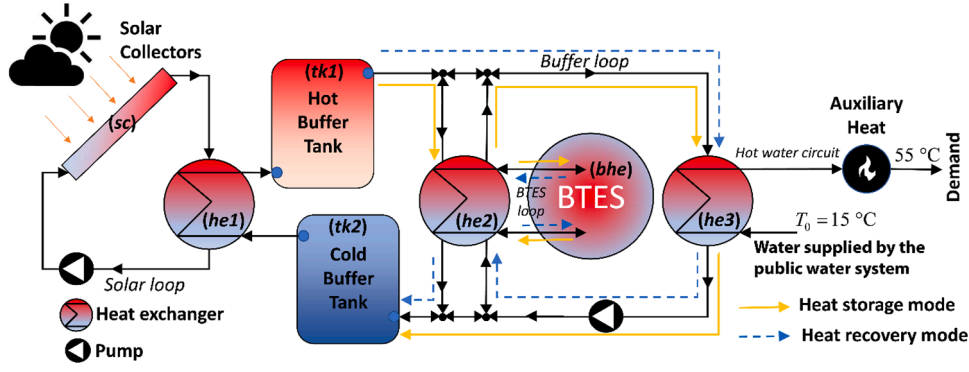
Fig. 11. Schematic diagram of the solar heating system with the indication of the heat storage mode and heat recovery mode flow paths. In the round brackets are reported the codes used in Appendix A to indicate the parameters and the state variables such as the temperature of each component of the solar heating system.

Table 1
Main technical specification of the solar heating system.

Parameter	Value
Vacuum pipe solar collectors	
Number of solar collectors	1,000
Adsorption surface of the single collector	3.02 m^2
1st order thermal dispersion coefficient	1.33 Wm^{-2}K^{-1}
2st order thermal dispersion coefficient	0.0067 Wm^{-2}K^{-2}
Optical efficiency	0.84
Liquid volume	1.65×10^{-3} m^3
Maximum temperature	95°C
Buffer Tank	
Volume	150 m^3
Internal diameter	5 m
Internal eight	7.64 m
Thickness	0.1 m
Thermal conductivity of walls	0.05 Wm^{-1}K^{-1}
Plate heat exchanger	
Number of plates	30
Plate surface	0.963 m^2
Plate thickness	5×10^{-4} m
Plate thermal conductivity	40 Wm^{-1}K^{-1}

the Adriatic Sea for a depth $\zeta > 15$ m below the MSL, whereas outflow condition is imposed at the discharge zone for a depth $\zeta \leq 15$ m below the MSL. At landward side, according to Eq. (1), constant flux corresponding to the recharge rate $Q_f = 0.6$ m^{2}d^{-1} was assigned for a depth $\zeta = 26.5$ m below the MSL. No flow condition was imposed along the other boundaries. Groundwater flow and solute transport is simulated until the flow and mass budget for the whole simulated domain reaches a constant value over time. Model results represent the existing hydrodynamic steady state condition of the aquifer. Successively, the effect of tidal fluctuation was considered. At seaward side the time series of the seawater level monitored at hourly scale in the period 2020–2021 in the tide station of Bari was imposed. Assuming that tidal fluctuations does not influence the fresh groundwater level at landward side, constant head corresponding to the groundwater level at steady state condition (0.90 m AMSL) was imposed.

According to the simulation results, the shallow freshwater aquifer flows with a maximum outflow specific discharge of 0.41 md^{-1} decreasing with the depth reaching its minimum value at 15 m AMSL. In correspondence of the transition zone, the inflow specific discharge from the sea reaches its maximum value equal to 0.089 md^{-1} decreasing with the depth according to the bulk permeability values. At depth higher than 150 m AMSL inflow specific discharge results lower than 1.56×10^{-3} md^{-1} (Fig. 9).

3.3. BTES design in the saltwater intrusion region

BTES design provides 12 branches composed by 3 BHEs connected in series (Fig. 10a). The upper part the borehole sections are thermally and hydraulically insulated in order to attenuate the thermal impact on the shallow fresh groundwater (Fig. 10b). Polyurethane foam with a thermal conductivity of 0.035 Wm^{-1}K^{-1} can be used as thermal insulator with watertight PVC pipe (Fig. 10c). Polyurethane may very well be a potential candidate for a BHE insulating grout and is already in use for sealing wellbores in other applications (Mansure 2002; Zawislanski and Faybishenko 1999). The heat exchange occurs only in the seawater intrusion region. Double U-tube vertical heat exchangers are installed in the boreholes with a diameter $D_b = 0.152$ m. Each U-tube is made of PEX with inner diameter $d_{pi} = 0.032$ m, outer diameter $d_{po} = 0.040$ m and thermal conductivity of 0.40 Wm^{-1}K^{-1}. The spacing of U-tube shanks is $D = 0.800$ m. Cement bentonite grout backfills the voids between the double U-tube heat exchanger and the borehole lateral surface presenting thermal conductivity of 2.0 Wm^{-1}K^{-1} (Fig. 10d).

The common measure of BTES efficiency is the Thermal Recovery Factor (*TRF*) which is the ratio between the heat recovered and the heat stored on the annual temporal scale. In particular way, in order to evaluate the effect of the thermal loss in the thermally insulated zone, the *TRF* was determined in two ways: as the ratio between the heat recovered (Q_{rec}) and heat stored (Q_{stor}) within BTES zone only (*TRF* = Q_{rec}/Q_{stor}); as the ratio between the effective heat recovered ($Q_{E,rec}$) and effective heat stored ($Q_{T,stor}$) into the subsurface (*TRF$_E$* = $Q_{E,rec}/Q_{E,stor}$).

3.4. Solar heating system

The Solar Heating System (SHS) is shown in Fig. 11. Solar irradiance, through the solar collectors, heats the fluid that flows in the solar loop. Then the solar loop exchanges heat with two buffer tanks filled with hot water and cold water in order to attenuate the daily thermal fluctuations. During heat storage mode, the hot buffer tank provides heated water to store energy in the BTES. Then it releases the remaining heat energy in the pool and DHW heating circuit. During the heat recovery mode, the hot water coming from hot buffer tank releases energy to the pool and DHW heating circuit first. Then it recovers heat from BTES. Table 1 shows the main features of the SHS. Freshwater fills the buffer tanks. Whereas water propylene glycol mixture (20% by volume) is used as heat carrier in both solar and BTES loop.

The performance of the SHS is measured with the determination of the efficiency of the SHS (η_{SHS}) which is the ratio between the thermal energy covered (Q_{cov}) and the thermal energy demand (Q_{thd}) determined at monthly scale.
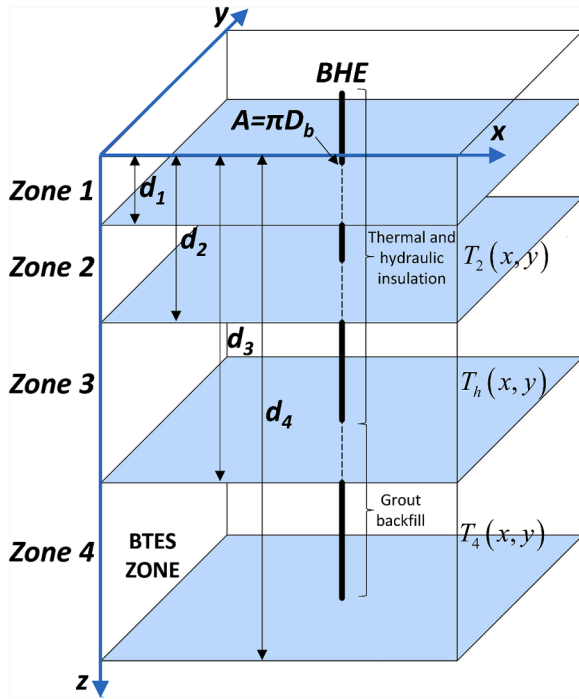
Fig. 12. Schematic representation of the hydrogeological structures consisting of 4 zones having different thicknesses.

3.5. Conceptual and computational model

A numerical model with different spatial scales was set up in COMSOL 4.0a environment to investigate the efficiency and the environmental behaviour of the borehole seasonal thermal storage system.

3.5.1. Working fluids

Thermophysical properties of working fluids vary with the state variables. Thermophysical properties of the water propylene glycol mixture as function of working temperature that flows into solar and BTES loop are derived from the Engineering Toolbox resources (https://www.engineeringtoolbox.com/propylene-glycol-d_363.html). Thermophysical properties of the groundwater as function of the temperature and salt concentrations as well as the freshwater that flows into buffer loop and in the hot water circuits are derived using the correlation functions disclosed by Nayar et al. (2016) and Shargawy et al. (2010).

3.5.2. Working conditions

According to the thermal heat demand of the USC and its weekly frequency of the customers, assuming that the temperature of the water supplied by the public water system is constant equal to 15°C and the temperature of the hot water to users must be 55°C, an estimation of the volumetric flow rate that circulates in the pool and DHW circuit $Q_d(t)$ (L^3T^{-1}) at hourly scale can be made. A logical function $\varphi(t)$ has been defined in order to represent the on/off flow conditions into the solar heating system:

$$\varphi(t) = (I(t) > 0)\|(Q_d(t) > 0) \tag{7}$$

Where $I(t)$ (WL^{-2}) is the solar net radiation. The heat carrier fluids in solar, buffer tank and BTES loop, flows until $\varphi(t) > 0$.

Another logical function $\delta(t)$ has been defined to represent the switch condition between the heat storage and recovery mode as:

$$\delta(t) = \begin{cases} 1 & \text{heat storage mode} \\ 0 & \text{heat recovery mode} \end{cases} \tag{8}$$

During the heat recovery mode, the volumetric flow rate that circulates

in solar, buffer tank and BTES loops $Q(t)$ (L^3T^{-1}) has been imposed equal to $Q_d(t)$. During heat storage mode, in order to store more solar energy, a constant value of the flow rate Q_0 (L^3T^{-1}) has been applied. Then, according to the above logical functions, the mass rate in the solar, buffer and BTES loop is given by:

$$Q(t) = Q_0\varphi(t)\delta(t) + Q_d(t)\varphi(t)(1 - \delta(t)) \tag{9}$$

Each component of the SHS is modelled with a set of non-linear ordinary differential equations. Details on the mathematical modeling can be found in Appendix A.

3.5.3. Quasi 3D conceptualization

The generic BHE crosses different geological and hydrogeological zones having different properties. Moreover, according to the BTES design, the BHE is constituted by a thermal and hydraulic insulated upper part and a cement bentonite backfilled lower part. Therefore, heat transfer occurs in different ways and rates along the depth. A quasi 3D conceptualization has been used in order to represent heat transfer in geological media. According to the geological and hydrogeological characterization and the BTES design, four homogeneous zones can be identified. Neglecting the interzone heat transfer (Karabetoglu et al., 2021), and assuming that the Rayleigh number remain always lower than its critical value, the three-dimensional subsurface heat transport can be divided into four two-dimensional heat transport problems.

In each zone is assumed that heat advection take place according to a constant average value of the inflow – outflow specific discharge determined on the basis of the results highlighted in Fig. 9.

A schematic view of BHE in the zoned hydrogeological structure consisting of 4 zones is given in Fig. 12.

The Zone 1 ($0 < z \leq d_1$) is the surficial unsaturated zone, where the temperature of the ground is mainly affected by the atmospheric condition. Since the depth d_1 is much lower than the depth d_4, the heat loss in the zone 1 can be neglected.

The Zone 2 ($d_1 < z \leq d_2$) is the shallow freshwater aquifer where the heat transfer is mainly influenced by advection phenomena due to the ground freshwater outflow specific discharge rate.

The Zone 3 ($d_2 < z \leq d_3$) corresponds to the part of the sealed BHE in the seawater intrusion region. Heat transfer is mainly influenced by heat conduction and advection due to the inflow specific discharge from the sea. Natural convection does not occur if Ra is lower than its critical value.

The Zone 4 ($d_3 < z < d_4$) is close to the part of cement bentonite backfilled BHE in the seawater intrusion region where heat storage and recovery of BTES system take place. Heat transfer takes place in in a similar way to the zone 3. Natural convection does not occur at Ra lower than Ra_c.

Details on the subsurface heat transfer model and the BTES model can be found in Appendix B.

4. Results

The goal of the present work is to assess the potentials and limitations of the BTES system into the seawater intrusion region. The following sections report the results of the methodologies applied for the design choices of the BTES system as well as to determine the working conditions and its efficiency. The conducted analysis should be viewed as proof concept analysis, and they are not to be considered exhaustive.

4.1. Choice design of BTES

According to the results of the previous sections, in order to avoid both natural convection and forced convection due to the temperature gradient and the groundwater flow, BTES must be installed deeper than 150 m AMSL where groundwater is in slow motion and bulk permeability has the lowest value.

Table 2

Summary of the operational conditions of the BTES according to baseline scenario.

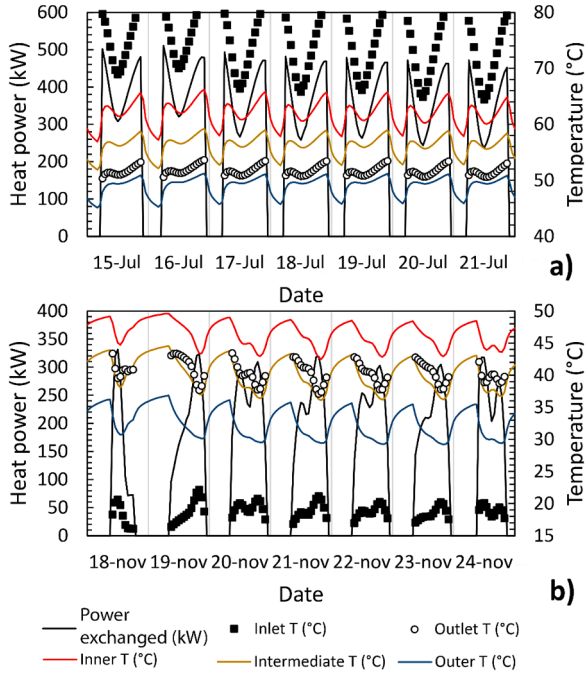|	Storage season	Recovery season
Period	04/15 - 10/15	10/16 - 04/14
Inlet temperature range (°C)	47.09 – 84.29	15.90 – 22.93
Outlet temperature range (°C)	36.10 -55.19	31.76 – 48.69
Max heat power exchanged (kW)	569	372
Max temperature at BHE wall (°C)	67.64	30.42
Max Rayleigh number (Ra$_{crit}$ = 4π^2)	30.73	

Fig. 13. Operational condition of the BTES. Power exchanged, inlet temperature, outlet temperature and temperature at borehole wall at inner, intermediate and outer zone during (a) storage season (15th – 21th July) (b) recovery season (18th – 24th November).

In fact, considering a maximum temperature T_b at borehole wall of 70°C, a value of the ambient Temperature of groundwater T_∞ of 18°C, a thermal diffusivity of the carbonate rock of 1.02×10^{-6} m^{2}s^{-1}, and a length L_{BHE} of the BTES of 100 m, the Rayleigh number Ra overcomes its critical values at a depth lower than 150 m AMSL where with a value of bulk permeability of 2.54×10^{-12} m^2 it reaches a value of 83.30.

At depth higher than 150 m AMSL, the bulk permeability decreases reaching a value of 1.02×10^{-12} m^2 corresponding to a value of the Ra of 33.47 lower than its critical value (Ra$_{crit}$ = 4π^2). Moreover, the inflow specific discharge decreases with the depth reaching a value lower than 1.56×10^{-3} md^{-1} for depths higher than 150 m AMSL.

For these reasons BHEs was thermally and hydraulically insulated up to the depth of 150 m AMSL and heat storage and recovery occurred at depth from 150 m to 250 m AMSL in order to preserve the lateral thermal stratification and minimize the advection heat loss.

4.2. Baseline scenario

According to the design choice, a baseline scenario was simulated. Hourly transient simulations are performed over a period of five years to assess the performance of the proposed energy system.

Operational conditions and efficiency of the BTES and solar heating system was examined using a constant annual heat storage and recovery cycle. The heat storage period of the BTES should be chosen on the basis
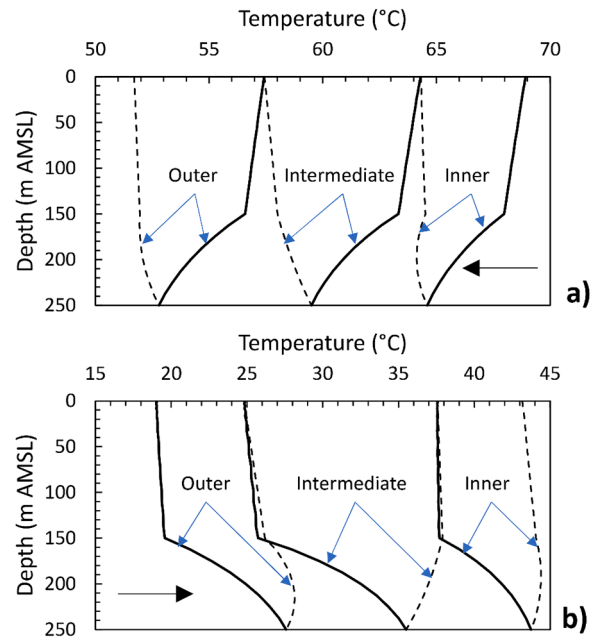
Fig. 14. Temperature profile of the heat carrier fluid within the BHEs at Outer, Intermediate, and Inner zone. Bold lines indicate the temperature profile within the inlet pipes. Dashed line indicates the temperature profile within outlet pipe. (a) storage season; (b) recovery season.
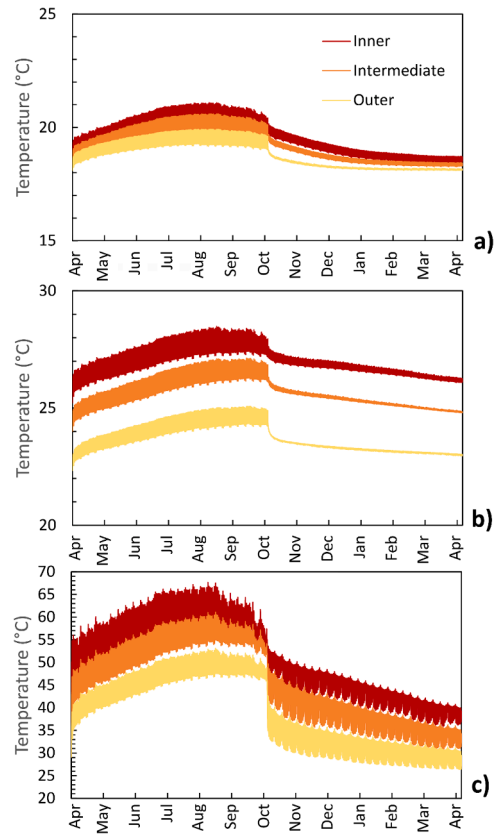
Fig. 15. Hourly temperature of aquifer in correspondence of borehole wall at Inner, Intermediate and Outer zones during the fifth year of operation. (a) Zone 2 (0 – 15 m AMSL); (b) Zone 3 (15 – 150 m AMSL); (c) Zone 4 (150 – 250 m AMSL).

Table 3
Operational condition of BTES at yearly scale with heat storage period from April 15th to October 15th.

Year	Q_{stor} (MWh)	Q_{ext} (MWh)	TRF	$Q_{E,stor}$ (MWh)	$Q_{E,ext}$ (MWh)	TRF_E
1	1105	305	0.28	1285	282	0.22
2	923	399	0.43	1103	375	0.34
3	850	439	0.52	1032	415	0.40
4	813	460	0.57	995	437	0.44
5	789	472	0.60	970	450	0.46

Q_{stor} (MWh) and Q_{ext} (MWh) is the heat stored and extracted within the BTES zone respectively, $TRF = Q_{stor}/Q_{ext}$ is the thermal recovery factor of the BTES, $Q_{E,stor}$ (MWh) and $Q_{E,ext}$ (MWh) are the total heat stored and extracted into the subsurface respectively, $TRF_E = Q_{E,stor}/Q_{E,ext}$ is the effective thermal recovery factor.
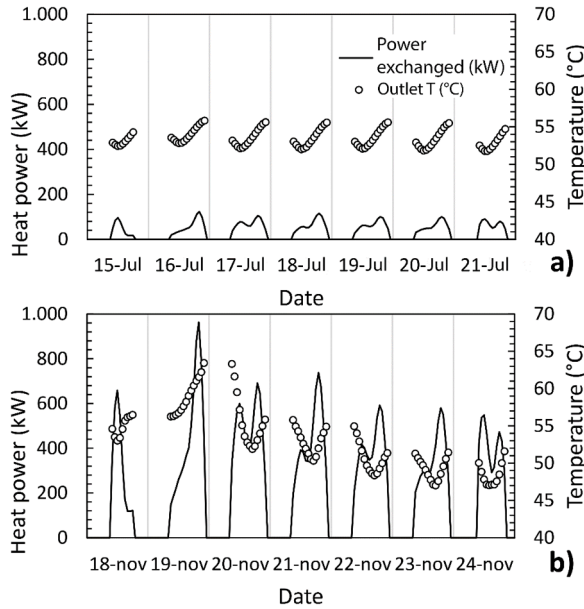

Fig. 16. Operational condition of the Solar Heating System. Heat power supply and outlet temperature at the hot water circuit of the USC during (a) storage season (15th–21th) July (b) recovery season (18th–24th November).

Table 4
Operational condition of the solar heating system at monthly scale.

	Q_{thd} (MWh)	$Q*_{cov}$ (MWh)	$\eta*_{SHS}$	Q_{cov} (MWh)	η_{SHS}
Jan	165	109	0.66	152	0.92
Feb	147	125	0.84	154	1.05
Mar	191	195	1.02	224	1.17
Apr	149	181	1.21	152	1.02
May	121	166	1.37	95	0.79
Jun	92	137	1.48	80	0.87
Jul	26	42	1.59	24	0.93
Aug	20	33	1.61	20	0.97
Sep	73	101	1.39	68	0.93
Oct	141	153	1.09	147	1.04
Nov	176	130	0.74	180	1.02
Dec	156	101	0.65	144	0.92

Q_{thd} (MWh) is the monthly thermal demand of the USC, $Q*_{cov}$ (MWh) and Q_{cov} (MWh) are the thermal energy covered without and with BTES respectively, $\eta*_{SHS} = Q_{thd}/Q*_{cov}$ and $\eta_{SHS} = Q_{thd}/Q_{cov}$ are the total efficiency of the Solar Heating System without and with BTES respectively.

of the trend of the monthly thermal demand of the USC that shows a substantial reduction in the period between May and September (Fig. 3). In the same period the monthly net solar radiation has a value higher than 150 kWh/m^2 (Fig. 4). On the basis of these considerations, the

Table 5
Operational condition of BTES at yearly scale changing the specific discharge, the maximum temperature of the solar collectors and the heating period respect to the baseline scenario.

	Years	Q_{stor} (MWh)	Q_{ext} (MWh)	TRF	e_{TRF} (%)	$T_{b,max}$ (°C)
Specific discharge (md^{-1})		**0.01**				
	1	1127	299	0.27	-3.85%	
	2	968	382	0.40	-8.65%	
	3	903	411	0.46	-11.78%	
	4	878	424	0.48	-14.54%	
	5	865	430	0,50	-16.81%	65.62
Max temperature of solar collectors (°C)		**75**				
	1	872	248	0.28	2.68%	
	2	723	319	0.44	1.94%	
	3	664	349	0.53	1.68%	
	4	638	365	0.57	1.14%	
	5	619	374	0.60	1.10%	56.05
Heat storage period		**05/15 - 09/15**				
	1	850	291	0.34	23.94%	
	2	759	383	0.51	16.74%	
	3	719	423	0.59	13.93%	
	4	699	444	0.64	12.34%	
	5	688	458	0.67	11.19%	64.45

Q_{stor} (MWh) and Q_{ext} (MWh) is the heat stored and extracted within the BTES zone respectively, $TRF = Q_{stor}/Q_{ext}$ is the thermal recovery factor of the BTES, e_{TRF} (%) is the percentange change on the TRF respect to the baseline scenario, $T_{b,max}$ (°C) is the maximum temperature at the borehole wall.

operational conditions of the system were examined for a heat storage period between April 15th and October 15th.

4.2.1. Operational condition and efficiency of BTES system

In the Table 2 are summarized the operational conditions of the BTES during the storage and recovery season. Fig. 13 shows the hourly operational condition of the BTES during the storage season from July 15th to July 21th (Fig. 13a) and during the recovery season from November 18th to November 24th (Fig. 13b).

During storage season the heat carrier fluid enters in the inner zone with a temperature in the range 47.09–84.24°C and exits from the outer zone with a temperature in the range 36.10–55.19°C.

Conversely, during the recovery season the cold heat carrier fluid enters in the outer zone with a temperature in the range 15.90–22.93°C and exits from the inner zone with a temperature in the range 31.76–48.69°C.

The heat power exchanged between the solar heating plant and the BTES varies according to the working condition.

During storage season, the heat carrier fluid flows within the BTES with a constant flow rate $Q_0 = 4.17 \times 10^{-3}$ m^{3}s^{-1} on the basis of the on/off flow condition (Eq. (7)). The heat power exchanged varies according to inlet and outlet temperature reaching a maximum value of 569 kW.

During recovery season, the flow rate of the heat carrier fluid within the BTES is the same of the hot water circuit which varies according to the frequency of the customers. The heat power exchanged is affected mainly by the flow variation reaching a maximum value of 372 kW.

Fig. 14 shows the temperature profile along the depth of the heat carrier fluid within the BHEs in correspondence of the inner, intermediate and outer zone of the BTES during the storage and recovery season. Within the thermally insulated zone, not negligible heat losses are evident. However, during the recovery season, the heat losses into the thermally insulated zone are mitigated, due to the fact that there is a smaller temperature differences between the heat carrier fluid and the thermal insulated zone.

As shown in Fig. 15, the thermal insulation attenuates the thermal impacts on the shallow freshwater aquifer. Its temperature does not
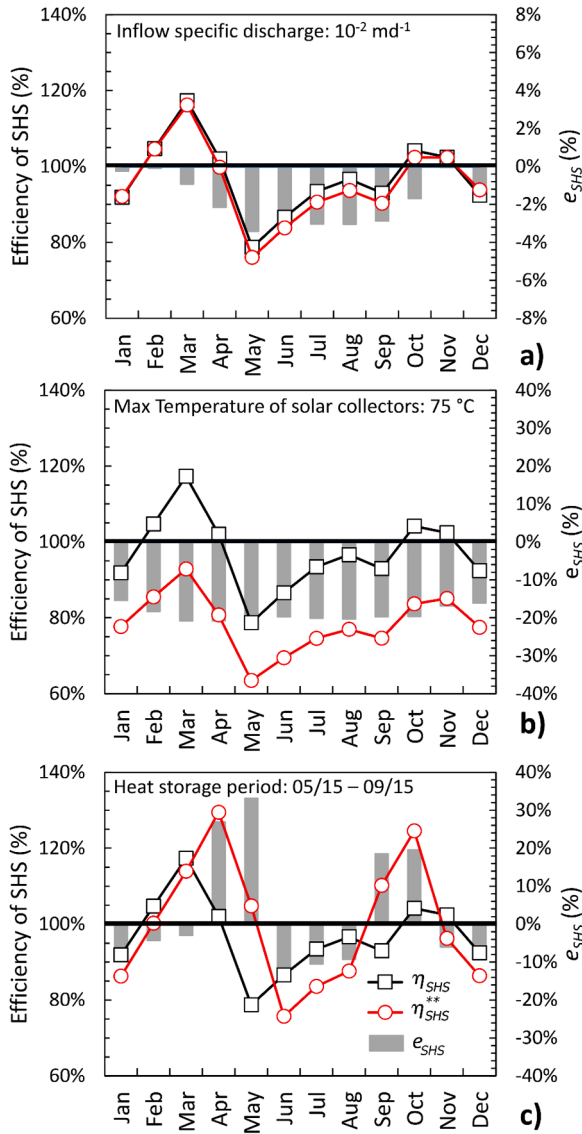
Fig. 17. Effect on the efficiency of the Solar Heating System at monthly scale at varying: (a) the specific discharge; (b) the maximum temperature of the solar collector; (c) the heat storage period respect to the baseline scenario. η_{SHS} (%) is the efficiency of SHS according to the baseline scenario, η^{**}_{SHS} (%) is the efficiency of the SHS according to the parameter changes, e_{SHS} (%) is the percentage change on η_{SHS} (%) respect to the baseline scenario.

exceed 21.1°C (Zone 2, 0–15 m AMSL). Whereas within the part of the thermally insulated BHEs in the sweater intrusion region the temperature does not exceed 28.5°C (Zone 3, 15–150 m AMSL) achieving to maximum value of 67.64°C within the BTES zone (Zone 4, 150–250 m AMSL).

Then, during the operational condition the temperature within the BTES zone does not exceed 67.64°C corresponding to a value of the maximum Ra number equal to 30.73 that is lower than its critical value ($Ra_{crit} = 4\pi^2$). Moreover, this condition does not permit the density driven flow from BTES zone to the upper zone because heat conduction remain stable and buoyancy forces are lower than the drag forces. As result the heated seawater remains confined in the BTES zone.

As shown in Table 3, the stored solar energy is not fully recovered. Storage and recovery cycles increase gradually the subsurface temperature at the BTES zone. As result the heat stored decreases and the heat recovered increases. Then *TRF* grows during the storage and recovery cycles towards to a steady state condition. It is clear that, the *TRF_E* is lower than the *TRF*. After 5 years of operation, the *TRF* of the BTES zone
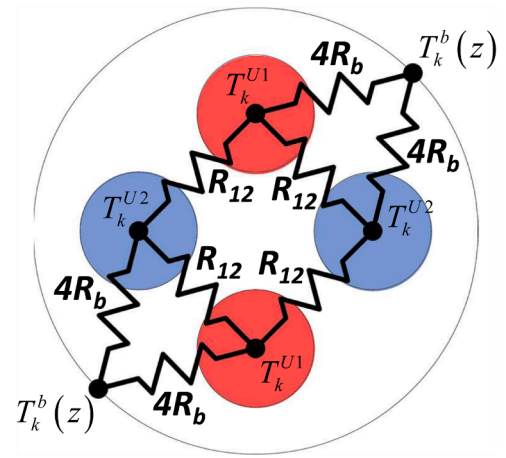

Fig. 18. Schematic representation of diagonal inlet and outlet pipes in grout borehole and the corresponding thermal network configuration involving the borehole thermal resistance R_b and the cross thermal resistance R_{12}.

is equal to 60%, whereas the TRF_E, due to the effect of the heat loss in the thermal insulated zone, reaches a value of 46 %.

Major differences are evident between the heat stored in the BTES zone Q_{stor} and the total heat stored in the subsurface $Q_{E,stor}$. After 5 years of operation, the ratio between the latter and the former is 0.81. Whereas the ratio between the heat recovered from BTES Q_{ext} zone and the effective heat recovered $Q_{E,ext}$ is 0.95.

4.2.2. Operational condition and efficiency of the Solar Heating System

Outlet temperature at the hot water circuit is more or less the required temperature (55°C) varying in the range 38.85–57.21°C during storage season and in the range 45.39–79.27°C during the recovery season. The heat power supply is modulated on the basis of the frequency of the customers. Fig. 16 shows the hourly operational condition of the SHS during the storage season from July 15th to July 21th (Fig. 16a) and during the recovery season from November 18th to November 24th (Fig. 16b).

Table 4 shows the comparison between the thermal energy demand, thermal energy covered and the total efficiency of the SHS at monthly scale considering the case where the BTES is not installed and the case where the BTES is installed.

As expected, for the first case the solar heating system during the spring and summer season produces a surplus of thermal energy and the efficiency of the SHS overcome the unit reaching a maximum value of 160.7%. During the fall and winter season efficiency decreases becoming lower the unit reaching the minimum value of 64.8% in December.

The installation of BTES permits to manage the solar heating production. During fall and winter season the efficiency of the SHS is higher going from 64.8% to 92.4% in December. During the spring and summer season the efficiency is lower variable between 78.7% in May and 96.6% in August.

4.3. Sensitivity analysis

Sensitivity analyses are used to evaluate how different operational and environmental conditions may influence the thermal recovery factor and solar heating system efficiency. The role of the inflow specific discharge, storage temperature and heat storage period were assessed.

4.3.1. Inflow specific discharge

BTES zone was in seawater region at depth higher than 150 m AMSL where groundwater flow is slow ($\sim 10^{-3}$ md^{-1}). Overlooking the increase of the bulk permeability, a shallower installation depth can permit to reduce the thermal losses in the thermally insulated zone but

at the same time the specific inflow discharge become higher. The performance of BTES zone with a value of a specific discharge equal to 10^{-2} md^{-1} was assessed.

A little decrease of the maximum temperature at borehole wall was observed (Table 5). Its value passes from 67.64°C to 65.62°C, whereas the *TRF* decreases of 16.81 % passing from 0.60 to 0.50 after five years of operation. As noticeable, the increase of the heat energy stored does not correspond with the increase of the heat energy recovered. After five years of operation Q_{stor} increases from 789 MWh to 865 MWh, whereas Q_{ext} decreases from 472 MWh to 430 MWh. As shown in Fig. 17a, this behaviour affects the efficiency of SHS. Anyway, a greater percentage change was evident during the storage season rather than the recovery season. Note that, during the storage season, in order to store more solar energy, the volumetric flow rate that circulates in the BTES loop is higher than the volumetric flow rate that circulates in the hot water circuit. Then, the increase of the specific discharge leads to a more heat energy dissipation. As consequence, the thermal demand covered by the SHS decreases. During the recovery season, less heat energy is recovered but its effect on the percentage change on η_{SHS} is less evident due to the fact that the volumetric flow rates that circulates in the BTES and in the hot water circuit are equal.

4.3.2. Storage temperature

In BTES zone the carbonate basement is more less fractured and karstified showing a value of bulk permeability lower than 10^{-12} m^2. According to the baseline scenario, the Ra number remains lower than its critical value (Ra = 30.73) and the heated seawater in BTES zone should not migrate to the upper zone. Due to natural heterogeneity of carbonate aquifer a larger safety margin should be desirable. A reduced value of maximum temperature of the solar collector from 95°C to 75°C was assessed. As expected, the maximum temperature at borehole wall decreases reaching a value of 56.05°C corresponding to a value of the Ra equal to 9.33. Less energy is stored in the BTES zone passing from 789 MWh to 619 MWh after five years of operation. However, *TRF* increases slightly of 1.10% in the fifth year (Table 5). As shown in Fig. 17b, significative percentage change is highlighted on the η_{SHS} which decreases considerably in the range 15.42%–20.82%.

4.3.3. Heat storage period

In real operational condition, the available net solar radiation and thermal demand may vary from year to year. Therefore, the system needs a modification of the annual storage and recovery cycle. The effect of a shorter heat storage period from May 15th to September 15th was assessed. The results show that the efficiency of BTES increases in the shortest heat storage period. The heat energy stored decreases but the capacity to recover heat increases. As shown in Table 5, after five years of operation the *TRF* increases by 11.19 %. However, a significative improvement on the efficiency of the SHS is not disclosed. As shown in Fig. 17c, a shorter heat storage period increases significantly η_{SHS} in the range of 18.54–33.13 % during the midseason (April – May and September-October), but at the same time, a moderate decrease is evident in the range of 9.33–12.59 % during summer season (June – August) and in the range of 4.31–6.53 % during the winter season (November – February).

5. Discussion

The goal of this study is to develop a framework to assess the potential and challenges of the solar BTES in a coastal aquifer. Thermal demands of the swimming pool and the DHW of the University Sport Centre (USC) located in the city of Bari (Italy) are used as benchmark, but the proposed analysis can be extended to the other sites with similar hydrogeological features.

The BTES design in terms of array configuration, numbers, spacing and depth of borehole is a critical aspect. Furthermore, the solar heating design in terms of the surface area of solar collectors, volume of buffer tank, etc. is also an important aspect. Another crucial factor is represented by the flow rate that circulates within the SHS and the BTES. The flow rate must be adequately modulated in order to satisfy the thermal energy demand and the operational constraints of the SHS and BTES. A trial and error approach was used to determine a satisfactory configuration on the basis of the numerical simulation results in terms of *TRF* and η_{SHS} subjected to environmental constraints. The best configuration of these design parameters and functions could be obtained by adopting optimization technique to achieve for instance the highest efficiency of heat extraction and the minimum total BHE length (Keshavarzzadeh et al., 2020; Shulte et al., 2016a; Cui et al., 2015). As known, the optimization requires several numerical simulations. The developed models based on the quasi – 3d conceptualizations reduce the required computational time for each simulation helping the design choice in the practical engineering purposes.

Among field factors influencing the *TRF* are the thermal diffusivity of the rock, the temperature differences between the ambient temperature and the temperature of the borehole walls, groundwater velocity and bulk permeability. The latter two factors play an important role on the design choice on positioning of the BTES.

As noticeable, groundwater advection was pointed out as a serious barrier to efficient BTES. In the case study, BTES is deeper than 150 m AMSL in order to minimize the advection loss due to the outflow specific discharge. As shown, the *TRF* decreases as the specific discharge increases. When the specific discharge is equal to the critical literature value of 10^{-2} md^{-1} outlined by Banks (2015), the *TRF* decreases passing from 0.6 to 0.5. On the other hand, a slight decrease of the maximum temperature at borehole wall from 67.64°C to 65.62°C and a moderate decrease of the η_{SHS} in the range 0.25–3.25 % are disclosed. Nguyen at al. (2017) approximately concur with this finding. The authors disclosed that for a value of specific discharge of 8.64×10^{-3} md^{-1} the outlet temperature from BTES is very similar to the case with no groundwater flow. Whereas the outlet temperature is considerably affected by the groundwater flow when the specific discharge results higher than 4×10^{-2} md^{-1}.

In the study area, at deeper than 150 m AMSL, the carbonate basement appears much less fractured and karstified. According to these observations, the hydraulic tests show that the bulk permeability decreases with the depth, reaching values lower than 1.0×10^{-12} m^2 at depth below 150 m AMSL making it suitable for BTES installation under the supposed maximum temperature of the borehole wall (~70°C). Lower bulk permeability maintains the Rayleigh number lower than its critical value. Then heat propagation occurs mainly by means of heat conduction in the seawater intrusion region preserving the lateral thermal stratification. This design choice agrees with the results presented by Catolico et al. (2016) that suggested a value of bulk permeability lower than 1.5×10^{-12} m^2 excluding natural convection heat losses (Ra lower than its critical value). Bär et al. (2015) adopted the same design criteria installing medium deep BTES at depth more than 100 m in order to find lower permeability. The classic Rayleigh stability criterion applied should be valid only for the homogeneous porous media. However, Graf and Thierren (2009) highlighted that this criterion can be applied on fractured rock when the fracture aperture is small. Mezon et al. (2018) disclose the existence of an equivalent Rayleigh number determined by a homogenization of fractured rock. Anyway, due to the natural heterogeneity and anisotropy which characterize the carbonate aquifer, the temperature at borehole wall may be reduced in order to have a more safety margin. As consequence, even if the *TRF* decreases slightly, less energy is stored and recovered at lower temperature. Then the efficiency of the SHS decreases. Benefit – cost analysis could be used to evaluate the opportunity of a detailed aquifer characterization in order to increase storage temperature maintaining the same safety margin.

The BHE design choice affects the thermal performance of the system. Double U-tube heat exchanger with high thermal conductivity of the grout (2.0 Wm^{-1}K^{-1}) ensures a good efficiency of heat exchange

between the borehole wall and the heat carrier fluid. The average values of the borehole thermal resistance R_b and the cross thermal resistance R_{12} are 0.0586 mKW^{-1} and 0.728 mKW^{-1}. Besides, thermal and hydraulic insulation zone constituted by plastic PVC pipe filled with polyurethane foam effectively prevents the heat losses and attenuates the thermal impacts on the shallow freshwater aquifer. The average values of R_b and R_{12} are much higher resulting equal to 2.913 mKW^{-1} and 8.958 mKW^{-1}. Despite the fact that the effective thermal resistance of BTES zone is lower than one order of magnitude of the effective thermal resistance of the thermal insulation zone, the thermal losses affect considerably the temperature profile of the heat carrier within the BTES (Fig. 14) as well as on the TRF_E (Table 3). According to the baseline scenario, after five years of operation the TRF_E is equal to 47 %. However, the found values of Thermal Recovery Factor are comparable with those presented by Sibbit et al. (2012) who investigated the performance of shallow BTES constituted by 144 BHEs of 30 m depth.

The efficiency of SHS reflects the ability of the BTES to govern the solar energy production. It plays an important role on the operational condition choices. A shorter heat storage period increases the TRF, but the efficiency of the SHS shows a more variable trend characterized by a surplus of thermal energy during the midseason and a deficit during the winter and summer season. As outlined by Rapantova et al. (2016) the effect of the duration of the heat storage period is not crucial for BTES operation.

The depth of installation of the BTES system is maintained lower than 250 m with the length of the thermally insulated zone and BTES zone equal to 150 m and 100 m respectively. As demonstrate by Welsh et al., 2016, a deeper BTES systems can store several GWh and extract a high TRF of up to 83%. However, the use of deeper borehole (>500 m) can have financial risk consequences. Under these circumstances, down the hole hydraulic hammer drilling technology should be used in order to have a vertical deviation angle less than 10 % (Bär et al. (2015). Nevertheless, to maintain the same investment costs, the increase of the borehole length should be accompanied by a reduction of the number of boreholes. As a consequence, the lateral thermal stratification may not be ensured reducing the efficiency of the heat extraction (Bär et al., 2015; Giordano and Raymond, 2019).

6. Conclusions

Storage and recovery of solar thermal energy in the seawater intrusion region underlying freshwater aquifers represents a new opportunity for beneficial use of these largely undeveloped groundwater resources for matching peak thermal energy production with peak thermal energy demand, especially in Mediterranean coastal areas where solar energy technology presents a great potential.

Installation of a BTES within seawater region with thermally and hydraulically insulated upper borehole section represents an environmental friendly design choice that prevent the thermal impact on the shallow freshwater aquifer. However thermal losses within the thermally insulated zone are not negligible and affect the Thermal Recovery Factor. Therefore, such system requires more heat storage and then a wider solar collector area. Detailed cost-benefit analysis is needed to determine the optimal techno-economic performance.

As outlined, the design choices of seasonal BTES are strongly depended on the operational conditions and the geological and hydrogeological context. The results obtained from this work suggest that site specific geological and hydrogeological characterization deserve a greater consideration in the BTES design.

Design choices in terms of BTES and solar heating system and their operational conditions required several iterative procedures. The developed conceptual, mathematical and numerical models allowed to solve simultaneously the complex time dependent dynamics involving the solar heating system and BTES together with the subsurface thermo-hydrogeological dynamics. The developed quasi 3d approach permits to reduce the computational time and at the same time to preserve an adequate realism of the hydrogeological conditions. The outlined model represents a tool for predicting and quantifying the thermal response and efficiency of BTES which may be used in experimental thermal response test analysis and BTES design. Future development concerns on the use of optimization algorithms to determine the best fit configuration of the plants in terms of the geometrical setup and operational conditions under the hydrogeological and environmental constraints.

Moreover, future activities should be directed towards the investigation of the role of the storage and recovery cycle at long-term temporal scale on the thermo-hydrogeologic features of the coastal aquifer. For instance, in carbonate aquifer the increases in temperature could favor the precipitation of calcium carbonate leading a clogging effect which reduces the permeability of fractured rock. A higher seawater temperature decreases both fluid density and viscosity and thus lowers the overall density contrast between the freshwater and seawater. This could make the freshwater-seawater interface retreats seaward and thus increase the freshwater storage. These aspect needs further insights and *in situ* experimentation.

CRediT authorship contribution statement

Nicola Pastore: Conceptualization, Methodology, Validation, Formal analysis, Investigation, Resources, Data curation, Writing – original draft, Writing – review & editing, Visualization, Supervision, Project administration, Funding acquisition. **Claudia Cherubini:** Validation, Investigation, Data curation, Writing – original draft, Writing – review & editing, Visualization.

Declaration of Competing Interest

The authors declare that they have no known competing financial interests or personal relationships that could have appeared to influence the work reported in this paper.

Acknowledgements

Appendix A

A.1. Solar collector

A solar vacuum pipe collector has been chosen. Assuming that heat carrier in the solar collector is completely mixed, according to Buzás et al. (1997), the energy balance of solar collector system can be expressed as:

$$\frac{d\left((\rho_l c_l)|_{T^{sc}} V^{sc} T^{sc}\right)}{dt} = I_n A^{sc} + (\rho_l c_l)|_{T_{in}^{sc}} Q(t) T_{in}^{sc} - (\rho_l c_l)|_{T^{sc}} Q(t) T^{sc} \tag{a.1}$$

Where the superscript *sc* stands for the solar collector, T_{in}^{sc} (K) is the inlet temperature, T^{sc} (K) is the outlet temperature, ρ_l (ML^{-3}) and c_l (L^{2}T^{-2}K^{-1}) are

the density and the heat capacity of the heat carrier fluid respectively, V^{sc} (L^3) is the volume of the heat carrier fluid within the solar collectors system, A^{sc} (L^2) is the total absorption surface, I_n (WL^{-2}) is the effective solar radiation transported by the heat carrier fluid given by (DIN EN 12975-1, 2022):

$$I_n = I\eta - k_1(T^{sc} - T_{ext}) - k_2(T^{sc} - T_{ext})^2 \tag{a.2}$$

Where η (-), k_1 (WL^{-2}K^{-1}) and k_2 (WL^{-2}K^{-2}) are the optical efficiency and the thermal dispersion coefficients of the solar collector.

A.2. Buffer Tanks.

A one-dimensional thermal stratification model was used to represent heat transfer processes. According to Nash et al. (2017), the hot buffer tank (*tk1*) and the cold buffer tank (*tk2*) was discretized with 6 nodes along its vertical axis to take account of the temperature stratification effect.

The conservation energy of the *j*-th node can be written as:

$$\frac{d\left((\rho_w c_w)|_{T_j^{tk}} V_j^{tk} T_j^{tk}\right)}{dt} = -\dot{Q}_{wall,j} + (\rho_w c_w)|_{T_{j+1}^{tk}} Q(t) T_{j+1}^{tk} - (\rho_w c_w)|_{T_j^{tk}} Q(t) T_j^{tk} - \dot{Q}_{j+1} + \dot{Q}_{j-1} \tag{a.3}$$

Where *tk* stands for buffer tank (*tk1* or *tk2*), T_j (K) is the temperature associated to the *j*-th node, ρ_w (ML^{-3}) and c_w (L^{2}T^{-2}K^{-1}) are the density and the specific heat capacity of the freshwater stored in the buffer tanks respectively, V_j^{tk} is the volume associated to the nodes *j*-th, $\dot{Q}_{wall,j}$ (W) is the heat loss due to the interaction between the tank wall and the ambient environment, $\dot{Q}_{-1}$ (W) and $\dot{Q}_{+1}$ (W) are the internal heat transfer rates solving with a finite difference scheme with temperature inversion correction method. $\dot{Q}_{wall,j}$, $\dot{Q}_{-1}$ and $\dot{Q}_{+1}$ is determined according to the methods illustrate in Nash et al. (2017).

A.3. Heat exchangers.

A plate heat exchanger has been chosen. The outlet temperature for the hot and cold fluid of the heat exchangers have been determined under the assumption of zero capacity heat exchanger and counter current flow condition with NTU - ε method (Çengel and Boles, 2008) solving the following equation:

$$T_{ho}^{he} - T_{hi}^{he} + \frac{\varepsilon \dot{Q}_{max}}{C_h} = 0$$
$$T_{co}^{he} - T_{ci}^{he} - \frac{\varepsilon \dot{Q}_{max}}{C_c} = 0 \tag{a.4}$$

Where *he* stands for heat exchanger (*he1, he2* or *he3*), T_{hi}^{he} (K) and T_{ho}^{he} (K) are the inlet and outlet temperature of the hot side, T_{ci}^{he} (K) and T_{co}^{he} (K) are the inlet and outlet temperature of the cold side, C_h (WK^{-1}) and C_c (WK^{-1}) are the heat capacity rates of the hot side and cold side respectively, $\dot{Q}_{max}$ (W) is the maximum heat power that can be exchanged. Heat exchanger effectiveness ε (-) was determined according to the methods illustrated by Çengel and Boles (2008).

The inlet temperatures of the hot and cold side of each heat exchanger (*he1, he2* and *he3*) are given by:

$$\begin{aligned}
T_{hi}^{he1} &= \min\left(T^{sc}, T_{max}^{sc}\right)\\
T_{ci}^{he1} &= T_{out}^{tk2}\\
T_{hi}^{he2} &= T_{ho}^{he3}\delta(t) - T_{out}^{tk1}(1-\delta(t))\\
T_{ci}^{he2} &= T_0\\
T_{hi}^{he3} &= T_{out}^{tk1}\delta(t) + T_{out}^{bhe}(1-\delta(t))\\
T_{ci}^{he3} &= T_{out}^{bhe}\delta(t) + T_{ho}^{he2}(1-\delta(t))
\end{aligned} \tag{a.5}$$

Where T_{max}^{sc} (K) is the maximum temperature allowed for the heat carrier fluid within the solar collector, T_{out}^{tk1} (K) and T_{out}^{tk2} (K) are the outlet temperature of the hot and cold buffer tank respectively, T_{out}^{bhe} (K) is the outlet temperature of the BTES system, T_0 (K) is the temperature of the public water system.

The outlet temperatures of the hot and cold side of each heat exchanger represent the inlet temperatures of the other components of the solar heating system (*sc, bhe, tk1* and *tk2*) and are given by:

$$\begin{aligned}
T_{in}^{sc} &= T_{ho}^{he1}\\
T_{in}^{tk1} &= T_{co}^{he1}\\
T_{in}^{bhe} &= T_{co}^{he3}\delta(t) + T_{ho}^{he3}(1-\delta(t))\\
T_{in}^{tk2} &= T_{ho}^{he2}\delta(t) + T_{co}^{he3}(1-\delta(t))\\
T_{in}^{aux} &= T_{co}^{he2}
\end{aligned} \tag{a.6}$$

Where T_{in}^{tk1} (K) and T_{in}^{tk2} (K) are the inlet temperatures of the hot and cold buffer tank respectively, T_{in}^{bhe} (K) is the inlet temperature of the BTES system, T_{in}^{aux} (K) is the inlet temperature of the auxiliary heat.

Appendix B

B.1. Subsurface heat transfer model

In a carbonate aquifer, rock matrix blocks and groundwater in the fracture network could have a different temperature due to the fast temperature changes (Frank et al., 2021). Anyway, due to the observation scale, the thermal equilibrium condition can be assumed. Then, heat transport in each zone is governed by the following equation:

$$(\rho c)_{eq} \frac{\partial T_h}{\partial t} - \nabla \cdot \left[-u_f \rho_w c_w T_h + \mathbf{K}_{eq} \nabla T_h \right] = 0 \qquad \text{(b.1)}$$

Where T_h (K) is the temperature of the generic h-th zone, u_f (LT^{-1}) is the inflow or outflow specific discharge aligned with the x direction, $(\rho c)_{eq}$ (ML^{-1}T^{-2}K^{-1}) and $\mathbf{K}_{eq}$ (ML^{3}T^{-2}K^{-1}) are the equivalent heat capacity and the equivalent thermal conductivity tensor respectively defined by the following expressions:

$$(\rho c)_{eq} = \theta \rho_w c_w + (1-\theta) \rho_m c_m \qquad \text{(b.2)}$$

$$\mathbf{K}_{eq} = \theta k_w + (1-\theta) k_m + \rho_w c_w \mathbf{D} \qquad \text{(b.3)}$$

Where θ (-) is the total porosity of rock, ρ_m (ML^{-3}), c_m (L^{2}T^{-2}K^{-1}), k_m (ML^{3}T^{-2}K^{-1}) are the density, heat specific capacity and thermal conductivity of the matrix block, ρ_m (ML^{-3}), c_w (L^{2}T^{-2}K^{-1}), k_w (ML^{3}T^{-2}K^{-1}) are the density, heat capacity and thermal conductivity of the groundwater, $\mathbf{D}$ (LT^{-2}) is the dispersion tensor as function of the specific discharge, the effective porosity θ_f, longitudinal and transverse dispersivity α_L (L) and α_T (L). The components of the dispersion tensor are given by:

$$D_{xx} = \alpha_L u_f / \theta_f; D_{yy} = \alpha_T u_f / \theta_f; D_{xy} = D_{yx} = 0 \qquad \text{(b.4)}$$

For each h-th zone, two-dimensional simulation area has a quadratic shape with the size of 100×100 m^2. The two-dimensional domain was aligned along the main flow path at USC. Constant ambient temperature and heat outflow boundary conditions were imposed in correspondence of the upward and downward flow boundaries respectively of the two-dimensional domains. BTES with geometry configuration highlighted in Fig. 10 is positioned at the center. In correspondence of the borehole wall with diameter D_b, a heat flux boundary condition has been imposed according to the BTES model presented in the following section.

Simulations has been performed on a two-dimensional finite element mesh for each h-th zone composed by 22114 triangles with element size between 0.04 and 20 m.

For each h-th zone and for each m-th borehole wall of a generic branch of the BTES system the average temperature can be determined as:

$$\overline{T}_{h,m} = \frac{\int_A T_h dA}{\pi D_b} \qquad \text{(b.5)}$$

B.2. BTES model

Each branch of the BTES system is linked with three double U-tube heat exchangers connected in series. The temperature along the borehole wall of each BHE is assumed uniformly distributed and varies along the depth. The U-tubes are arranged symmetrically with diagonal inlet pipes configurations. Heat transfer within BHE has been conceptualized with a quasi 3D model. The convective heat flow along the inlet and outlet pipes is close to the conductive heat flows among the heat carrier fluid and the borehole walls according to the thermal resistance network highlighted in Fig. 11. The borehole thermal resistance R_b (LKW^{-1}) and the cross thermal resistance R_{12} (LKW^{-1}) have been determined on the basis of the geometrical configuration of the BHE, and the thermophysical parameters of the BHE and the carbonate aquifer according to Claesson and Javed (2019). Moreover, both R_b and R_{12} are functions of the pipe resistance R_p (LKW^{-1}) which depends on the pipe flow condition. According to the method presented in Pastore et al. (2021b), R_p is determined as:

$$R_p = 1/\pi d_o h_{ext} \qquad \text{(b.6)}$$

Where h_{ext} (WL^{-2}K^{-1}) is the heat transfer coefficient including internal film resistance and the pipe wall resistance.
Fig. 18.

Temperature distribution along the z direction of the inlet and outlet pipes of the k-th double U-tube heat exchanger of the generic branch of the BTES is governed by the following equations:

$$\left(m_l^U c_l \right)_k \frac{dT_k^{U1}}{dz} + \frac{1}{2R_b} \left(T_k^{U1} - T_k^b(z) \right) + \frac{4}{R_{12}} \left(T_k^{U1} - T_k^{U2} \right) = 0$$

$$\left(m_l^U c_l \right)_k \frac{dT_k^{U2}}{dz} + \frac{1}{2R_b} \left(T_k^{U2} - T_k^b(z) \right) + \frac{4}{R_{12}} \left(T_k^{U2} - T_k^{U1} \right) = 0 \qquad \text{(b.7)}$$

Subjected to the following boundary conditions:

$$\begin{aligned}
T_1^{U1}(d_1, t) &= T_{in}^{BHE} k = 1 \\
T_k^{U1}(d_1, t) &= T_{k-1}^{U2}(d_1, t) k = 2, 3 \\
T_k^{U2}(d_4, t) &= T_k^{U1}(d_4, t) k = 1, 2, 3
\end{aligned} \qquad \text{(b.8)}$$

Where m_l^U (MT^{-1}) and c_l (L^{2}T^{-2}K^{-1}) are the mass flow rate and the specific heat of the heat carrier fluid that flows within the k-th double U-tube heat exchanger, T_k^{U1} (K) and T_k^{U2} (K) are the temperatures along the inlet and outlet pipes of the double U-tube heat exchanger, $T_k^b(z)$ (K) is the temperature of the borehole wall.

The local heat flux along the depth of the k-th borehole wall $\dot{q}_k$ (WL^{-2}) is given by:

$$\dot{q}_k = \frac{1}{R_b} \left(\frac{T_k^{U1} + T_k^{U2}}{2} - T_k^b(z) \right) \qquad \text{(b.9)}$$

For each generic branch of the BTES Eq. (22) subjecting to the boundary condition of Eq. (23) has been solved along one – dimensional domain having

the length $d_4 - d_1$ discretized with linear elements with maximum element size of 10 m.

B.3. Coupling between the BTES and subsurface heat transfer model

Coupling boundary conditions between the subsurface heat transfer model and the BTES model is needed. Coupling model takes into account of the change of the working condition from heat storage mode ($\delta(t) = 1$) to heat recovery mode ($\delta(t) = 0$).

During the heat recovery mode, for each branch, the inner and outer double U-tube heat exchanger switch their position. In this manner, during the heat storage mode hot temperature enters in the inner double U-tube heat exchangers, conversely during the heat recovery mode cold temperature enters in the outer double U-tube heat exchangers.

In the subsurface heat transfer model, for each h-th zone and for each m-th borehole wall belong the generic branch, a heat flux boundary condition has been imposed according to the following equation:

$$\dot{q}_{h,m} = \delta(t)\dot{q}_{h,k} + (1 - \delta(t))\dot{q}_{h,3-k+1} \tag{b.10}$$

Where $\dot{q}_{h,m}$ (WL^{-2}) is the heat flux imposed to the m-th borehole wall of the generic branch in the h-th zone, $\dot{q}_{h,k}$ (WL^{-2}) is the averaged local heat flux of the k-th double U-tube heat exchanger determined in correspondence of the h-th zone given by:

$$\dot{q}_{h,k} = \frac{\int_{d_{h-1}}^{d_h} \dot{q}_k dz}{\pi D_b(d_h - d_{h-1})} \tag{b.11}$$

In the BTES model for the generic branch, the temperature of the k-th borehole wall is given by:

$$T_k^b(z) = \sum_{h=2}^{4} T_{h,k}^b \cdot (d_{h-1} < z < d_h) \tag{b.12}$$

Where $T_{h,k}^b$ (K) is the temperature of the k-th borehole wall at the h-th zone determined as:

$$T_{h,k}^b = \delta(t)\overline{T}_{h,m} + (1 - \delta(t))\overline{T}_{h,3-m+1} \tag{b.13}$$

The outlet temperature from the BTES system T_{out}^{bhe} is determined as the mean of the outlet temperature of $k=3$ BHE of each branch ($T_3^{U2}(0,t)$).

References

Abbas, Z., Chen, D., Li, Y., Yong, L., Wang, R.Z., 2020. Experimental investigation of underground seasonal cold energy storage using borehole heat exchangers based on laboratory scale sandbox. Geothermics 87 (November 2019). https://doi.org/10.1016/j.geothermics.2020.101837.

Banks, D., 2015. A review of the importance of regional groundwater advection for ground heat exchange. Environ. Earth Sci. 2555–2565 https://doi.org/10.1007/s12665-014-3377-4.

Bär, K., Rühaak, W., Welsch, B., Schulte, D., Homuth, S., Sass, I., 2015. Seasonal high temperature heat storage with medium deep borehole heat exchangers. Energy Procedia 76, 351–360. https://doi.org/10.1016/j.egypro.2015.07.841.

Beckers, K.F., Rangel-Jurado, N., Chandrasekar, H., Hawkins, A.J., Fulton, P.M., Tester, J.W., 2022. Techno-economic performance of closed-loop geothermal systems for heat production and electricity generation. Geothermics 100, 102318. https://doi.org/10.1016/j.geothermics.2021.102318.

Bloemendal, M., Olsthoorn, T., 2018. ATES systems in aquifers with high ambient groundwater flow velocity. Geothermics 75 (January), 81–92. https://doi.org/10.1016/j.geothermics.2018.04.005.

Borgia, G.C., Bortolotti, V., Masciopinto, C., 2002. Valutazione del contributo della porosità effettiva alla trasmissività di acquiferi fratturati con tecniche di laboratorio e di campo. Ingegneria e Geologia degli Acquiferi 17, 31–43. IGEA.

Buzás, J., Farkas, I., Biró, A., Németh, R., 1997. Modelling and simulation of a solar thermal system. IFAC Proc. Vol. 30 (5), 143–147. https://doi.org/10.1016/s1474-6670(17)44423-5.

Burns, E.R., Bershaw, J., Williams, C.F., Wells, R., Uddenberg, M., Scanlon, D., Cladouhos, T., van Houten, B., 2020. Using saline or brackish aquifers as reservoirs for thermal energy storage, with example calculations for direct-use heating in the Portland Basin, Oregon, USA. Geothermics 88 (May), 101877. https://doi.org/10.1016/j.geothermics.2020.101877.

Catolico, N., Ge, S., McCartney, J.S., 2016. Numerical modeling of a soil-Borehole Thermal Energy Storage System. Vadose Zone J. 15 (1), 1–17. https://doi.org/10.2136/vzj2015.05.0078.

Çengel, Y.A., Boles, M.A., 2008. Introduction to Thermodynamics and Heat Transfer, 2nd Edition. McGraw-Hill, Boston.

Cherubini, C., Giasi, C., Pastore, N., 2013. Fluid flow modeling of a coastal fractured karstic aquifer by means of a lumped parameter approach. Environ. Earth Sci. 70 (5), 2055–2060. https://doi.org/10.1007/s12665-010-0851-5.

Cherubini, C., Pastore, N., Rapti, D., Giasi, C.I., 2018. Numerical modeling of flow and transport in the Bari industrial area by means of rough walled parallel plate and random walk models. Hydrol. Earth Syst. Sci. 22 (10), 5211–5225. https://doi.org/10.5194/hess-22-5211-2018.

Claesson, J., Javed, S., 2019. Explicit multipole formulas and thermal network models for calculating thermal resistances of double U-pipe borehole heat exchangers. Sc. Technol. Built Environ. 25 (8), 980–992. https://doi.org/10.1080/23744731.2019.1620565.

Cui, P., Diao, N., Gao, C., Fang, Z., 2015. Thermal investigation of in-series vertical ground heat exchangers for industrial waste heat storage. Geothermics 57, 205–212. https://doi.org/10.1016/j.geothermics.2015.06.003.

Di Sipio, E., Galgaro, A., Destro, E., Giaretta, A., Chiesa, S., VIGOR Team, 2016. Thermal conductivity of rocks and regional mapping. In: European Geothermal Congress Pisa. Italy 3–7 June 2013.

Diersch, H.J.G., 2014. FEFLOW Finite element modeling of flow, mass and heat transport in porous and fractured media. Springer, Berlin Heidelberg, Berlin.

DIN EN 12975-1. Thermal solar systems and components - Solar collectors - Part 1: General requirements (includes Amendment A1:2010).

Frank, S., Heinze, T., Pollak, S., Wohnlich, S., 2021. Transient heat transfer processes in a single rock fracture at high flow rates. Geothermics 89, 101989. https://doi.org/10.1016/j.geothermics.2020.101989.

Giordano, N., Raymond, J., 2019. Alternative and sustainable heat production for drinking water needs in a subarctic climate (Nunavik, Canada): Borehole Thermal Energy Storage to reduce fossil fuel dependency in off-grid communities. Appl. Energy 252 (December 2018), 113463. https://doi.org/10.1016/j.apenergy.2019.113463.

Graf, T., Therrien, R., 2009. Stable-unstable flow of geothermal fluids in fractured rock. Geofluids 9 (2 SPEC. ISS), 138–152. https://doi.org/10.1111/j.1468-8123.2008.00233.x.

Grassi, D., Sdao, F., Tadolini, T, 1986. Idrogeologia dell'area posta a cavallo della Murgia e del Tavoliere di Puglia. Geol. Appl. Idro XXI, 85–98.

Houben, G.J., 2015. Review: hydraulics of water wells—flow laws and influence of geometry. Hydrogeol. J. 23 (8), 1633–1657. https://doi.org/10.1007/s10040-015-1312-8.

Karabetoglu, S., Ozturk, Z.F., Kaslilar, A., Juhlin, C., Sisman, A., 2021. Effect of layered geological structures on borehole heat transfer. Geothermics 91 (November 2020), 102043. https://doi.org/10.1016/j.geothermics.2021.102043.

Keshavarzzadeh, A.H., Maleki Zanjani, A., Gharali, K., Dusseault, M.B., 2020. Multi-objective evolutionary-based optimization of a ground source heat exchanger geometry using various optimization techniques. Geothermics 86 (April), 101861. https://doi.org/10.1016/j.geothermics.2020.101861.

Klein, S.A., Beckman, W.A., Mitchell, J.W., Duffie, J.A., Duffie, N.A., Freeman, T.L., et al. (2017) TRNSYS 18: A Transient System Simulation Program.

Lancaster-Jones, P.F.F., 1975. The interpretation of the Lugeon water-test. Q. J. Eng. Geol. Hydrogeol. 8 (2), 151–154. https://doi.org/10.1144/GSL.QJEG.1975.008.02.05.

Langevin, C.D., Thome Jr., D.T., Dausman, A.M., Sukop, M.C., Guo, W., 2008. SEAWAT Version 4: A Computer Program for Simulation of Multi–Species Solute and Heat Transport. U.S. Geological Survey Techniques and Methods 6–A22, 2008; Volume 39. Availableonline. https://pubs.usgs.gov/tm/tm6a22/ (accessed on 12 March 2021).

Ma, Q., Wang, P., 2020. Underground solar energy storage via energy piles. Appl. Energy 261 (January), 114361. https://doi.org/10.1016/j.apenergy.2019.114361.

Mansure, AJ, 2002. In: Polyurethane grouting geothermal lost circulation zones. Paper presented at the IADC/SPE Drilling Conference. Dallas, Texas, 26–28 Feb 2002.

Masciopinto, C., 2006. Simulation of coastal groundwater remediation: the case of Nardò fractured aquifer in Southern Italy. Environ. Model. Softw. 21 (1), 85–97. https://doi.org/10.1016/j.envsoft.2004.09.028.

Masciopinto, C., Palmiotta, D., 2016. A new method to infer advancement of saline front in coastal groundwater systems by 3D: the case of Bari (Southern Italy) fractured aquifer. Computation 4, 9. https://doi.org/10.3390/computation4010009.

Mezon, C., Mourzenko, V.V., Thovert, J.F., Antoine, R., Fontaine, F., Finizola, A., Adler, P.M., 2018. Thermal convection in three-dimensional fractured porous media. Phys. Rev. E 97 (1). https://doi.org/10.1103/PhysRevE.97.013106.

Moradi, A., Smits, K.M., Massey, J., Cihan, A., McCartney, J., 2015. Impact of coupled heat transfer and water flow on soil Borehole Thermal Energy Storage (SBTES) Systems: experimental and modeling investigation. Geothermics 57, 56–72. https://doi.org/10.1016/j.geothermics.2015.05.007.

Nash, A.L., Badithela, A., Jain, N., 2017. Dynamic modeling of a sensible thermal energy storage tank with an immersed coil heat exchanger under three operation modes. Appl. Energy 195, 877–889. https://doi.org/10.1016/j.apenergy.2017.03.092.

Nayar, K.G., Sharqawy, M.H., Banchik, L.D., Lienhard, V, 2016. Thermophysical properties of seawater: a review and new correlations that include pressure dependence. Desalination 390, 1–24. https://doi.org/10.1016/j.desal.2016.02.024.

Nguyen, A., Pasquier, P., Marcotte, D., 2017. Borehole Thermal Energy Storage Systems under the influence of groundwater flow and time-varying surface temperature. Geothermics 66, 110–118. https://doi.org/10.1016/j.geothermics.2017.04.002.

Niederau, J., Ebigbo, A., Marquart, G., Mendoza, S.G., Inversi, B., Gola, G., Scrocca, D., Manzella, A., Montegrossi, G., Clauser, C., 2015. Assessment and Simulation of Various Utilization Scenarios of a Medium-Enthalpy Reservoir in Southern Italy (Guardia Lombardi). In: *World Geothermal Congress 2015, April*, 9.

Nield, D.A., Bejan, A., 2013. Convection in porous media. Springer, New York, NY. https://doi.org/10.1007/978-1-4614-5541-7.

Nordell, B, Snijders, A, Stiles, L., 2015. The use of aquifers as thermal energy storage (TES) systems. editor. In: Cabeza, LF (Ed.), Advances in Thermal Energy Storage Systems. Elsevier, pp. 87–115.

Nouri, G., Noorollahi, Y., Yousefi, H., 2019. Designing and optimization of solar assisted ground source heat pump system to supply heating, cooling and hot water demands. Geothermics 82 (March), 212–231. https://doi.org/10.1016/j.geothermics.2019.06.011.

Panja, P., McLennan, J., Green, S., 2021. Influence of permeability anisotropy and layering on geothermal battery energy storage. Geothermics 90 (November 2020), 101998. https://doi.org/10.1016/j.geothermics.2020.101998.

Pastore, N., Cherubini, C., Giasi, C.I., 2021b. Analysis of gravel back-filled borehole heat exchanger in karst fractured limestone aquifer at local scale. Geothermics 89, 101971. https://doi.org/10.1016/j.geothermics.2020.101971.

Pastore, N., Cherubini, C., Giasi, C.I., Rapti, D., 2021a. Numerical model of the behavior of chlorinated ethenes in a fractured, karstic limestone aquifer. Hydrol. J. https://doi.org/10.1007/s10040-020-02248-1.

Pieri, P., Sabato, L., Spalluto, L., and Tropeano, M.: Note Illustrative della Carta Geologica d'Italia alla scala 1 V 50:000 foglio 438, Bari, Nuova Carta Geologica d'Italia alla scala 1 V 50:000– Progetto CARG, ISPRA-Servizio Geologico d'Italia, ISBN 2035-8008, January 2012.

Pu, L., Xin, P., Nguyen, T.T.M., Yu, X., Li, L., Barry, D.A., 2020. Thermal effects on flow and salinity distributions in coastal confined aquifers. Water Resour. Res. 56 https://doi.org/10.1029/2020WR027582 e2020WR027582.

Rapantova, N., Pospisil, P., Koziorek, J., Vojcinak, P., Grycz, D., Rozehnal, Z., 2016. Optimisation of experimental operation of Borehole Thermal Energy Storage. Appl. Energy 181, 464–476. https://doi.org/10.1016/j.apenergy.2016.08.091.

Robertson, E.C., 1988. Thermal Properties of Rocks. US Department of the Interior: Geological Survey, pp. 88–441.

Sakellariou, E.I., Wright, A.J., Axaopoulos, P.J., 2021. Energy, economic and emission assessment of a solar assisted shallow earth borehole field heat pump system for domestic space heating in a north European climate. Geothermics 95 (May), 102159. https://doi.org/10.1016/j.geothermics.2021.102159.

Schulte, D.O., Rühaak, W., Oladyshkin, S., Welsch, B., Sass, I., 2016a. Optimization of Medium-Deep Borehole Thermal Energy Storage Systems. Energy Technol. 4 (1), 104–113. https://doi.org/10.1002/ente.201500254.

Schulte, D.O., Welsch, B., Boockmeyer, A., Rühaak, W., Bär, K., Bauer, S., Sass, I., 2016b. Modeling insulated borehole heat exchangers. Environ. Earth Sci. (10), 75. https://doi.org/10.1007/s12665-016-5638-x.

Schulte, D. O., Welsch, B., Formhals, J., and Sass, I. (2019). Potentials and challenges of borehole thermal energy storage in solar district heating grids. 11–14.

Schüppler, S., Fleuchaus, P., Blum, P., 2019. Techno-economic and environmental analysis of an Aquifer Thermal Energy Storage (ATES) in Germany. Geotherm. Energy 7 (1). https://doi.org/10.1186/s40517-019-0127-6.

Sharqawy, M.H., V, J.H.L., Zubair, S.M, 2010. Thermophysical properties of seawater: a review of existing correlations and data. Desalination and Water Treat. 16 (1–3), 354–380. https://doi.org/10.5004/dwt.2010.1079.

Sheldon, H.A., Wilkins, A., Green, C.P., 2021. Recovery efficiency in high-temperature aquifer thermal energy storage systems. Geothermics 96 (May), 102173. https://doi.org/10.1016/j.geothermics.2021.102173.

Sibbitt, B., McClenahan, D., Djebbar, R., Thornton, J., Wong, B., Carriere, J., Kokko, J., 2012. The performance of a high solar fraction seasonal storage district heating system - five years of operation. Energy Procedia 30, 856–865. https://doi.org/10.1016/j.egypro.2012.11.097.

Skarphagen, H., Banks, D., Frengstad, B. S., and Gether, H. (2019). Review Article Design Considerations for Borehole Thermal Energy Storage (BTES): A Review with Emphasis on Convective Heat Transfer. 2019.

Spitler, J.D., Javed, S., Ramstad, R.K., 2016. Natural convection in groundwater-filled boreholes used as ground heat exchangers. Appl. Energy 164, 352–365. https://doi.org/10.1016/j.apenergy.2015.11.041.

Vaskou, P., de Quadros, E.F., Kanji, M.A., Johnson, T., Ekmekci, M., 2019. ISRM suggested method for the Lugeon test. Rock Mech. Rock Eng. 52 (10), 4155–4174. https://doi.org/10.1007/s00603-019-01954-x.

Wang, K., Herrando, M., Pantaleo, A.M., Markides, C.N., 2019. Technoeconomic assessments of hybrid photovoltaic-thermal vs. conventional solar-energy systems: case studies in heat and power provision to sports centres. Appl. Energy 254 (August), 113657. https://doi.org/10.1016/j.apenergy.2019.113657.

Welsch, B., Göllner-Völker, L., Schulte, D.O., Bär, K., Sass, I., Schebek, L., 2018. Environmental and economic assessment of Borehole Thermal Energy Storage in district heating systems. Appl. Energy 216 (October 2017), 73–90. https://doi.org/10.1016/j.apenergy.2018.02.011.

Welsch, B., Rühaak, W., Schulte, D.O., Bär, K., Sass, I., 2016. Characteristics of medium deep Borehole Thermal Energy Storage. Int. J. Energy Res. 40, 1855–1868. https://doi.org/10.1002/er.3570.

Werner, S., 2017. International review of district heating and cooling. Energy 137, 617–631. https://doi.org/10.1016/j.energy.2017.04.045.

Winterleitner, G., Schütz, F., Wenzlaff, C., Huenges, E., 2018. The Impact of Reservoir Heterogeneities on High-Temperature Aquifer Thermal Energy Storage Systems. A Case Study from Northern Oman. Geothermics 74 (November 2017), 150–162. https://doi.org/10.1016/j.geothermics.2018.02.005.

Zawislanski, PT, Faybishenko, B, 1999. New casing and backfill design for neutron logging access boreholes. Ground Water 37, 33–37. https://doi.org/10.1111/j.1745-6584.1999.tb00955.x.

Zeghici, R.M., Oude Essink, G.H.P., Hartog, N., Sommer, W., 2015. Integrated assessment of variable density-viscosity groundwater flow for a high temperature mono-well aquifer thermal energy storage (HT-ATES) system in a geothermal reservoir. Geothermics 55, 58–68. https://doi.org/10.1016/j.geothermics.2014.12.006.

Zhou, C.B., Zhao, X.J., Chen, Y.F., Liao, Z., Liu, M.M., 2018. Interpretation of high pressure pack tests for design of impervious barriers under high-head conditions. Eng. Geol. 234 (January), 112–121. https://doi.org/10.1016/j.enggeo.2018.01.006.